

TransMorph: Transformer for unsupervised medical image registration

Junyu **Chen**^{a,b,*}, Yong **Du**^a, Yufan **He**^e, William P. **Segars**^c, Ye **Li**^d, Eric C. **Frey**^{a,b}

^a*Russell H. Morgan Department of Radiology and Radiological Science, Johns Hopkins Medical Institutes, Baltimore, MD, USA*

^b*Department of Electrical and Computer Engineering, Johns Hopkins University, Baltimore, MD, USA*

^c*Carl E. Ravin Advanced Imaging Laboratories, Department of Radiology, Duke University Medical Center, Durham, NC, USA*

^d*Center for Advanced Medical Computing and Analysis, Massachusetts General Hospital and Harvard Medical School, Boston, MA, USA*

^e*NVIDIA Corporation, Bethesda, MD, USA*

ARTICLE INFO

Article history:

Received xx xx 20xx

Received in final form xx xx 20xx

Accepted xx xx 20xx

Available online xx xx 20xx

ABSTRACT

In the last decade, convolutional neural networks (ConvNets) have dominated the field of medical image analysis. However, it is found that the performances of ConvNets may still be limited by their inability to model long-range spatial relations between voxels in an image. Numerous vision Transformers have been proposed recently to address the shortcomings of ConvNets, demonstrating state-of-the-art performances in many medical imaging applications. Transformers may be a strong candidate for image registration because their self-attention mechanism enables a more precise comprehension of the spatial correspondence between moving and fixed images. In this paper, we present TransMorph, a hybrid Transformer-ConvNet model for volumetric medical image registration. We also introduce three variants of TransMorph, with two diffeomorphic variants ensuring the topology-preserving deformations and a Bayesian variant producing a well-calibrated registration uncertainty estimate. The proposed models are extensively validated against a variety of existing registration methods and Transformer architectures using volumetric medical images from two applications: inter-patient brain MRI registration and phantom-to-CT registration. Qualitative and quantitative results demonstrate that TransMorph and its variants lead to a substantial performance improvement over the baseline methods, demonstrating the effectiveness of Transformers for medical image registration.

1. Introduction

Deformable image registration (DIR) is fundamental for many medical imaging analysis tasks. It functions by establishing spatial correspondence in order to minimize the differences between a pair of fixed and moving images. Traditional methods formulate image registration as a variational problem for estimating a smooth mapping between the points in one image and those in another (Avants et al. 2008; Beg et al. 2005; Vercauteren et al. 2009; Heinrich et al. 2013a; Modat et al. 2010). However, such methods are computationally expensive and usually slow in practice because the optimization problem needs to be solved from scratch for each pair of unseen images.

Since recently, deep neural networks (DNNs), especially convolutional neural networks (ConvNets), have demonstrated

state-of-the-art performances in many computer vision tasks, including object detection (Redmon et al. 2016), image classification (He et al. 2016), and segmentation (Long et al. 2015). Ever since the success of U-Net in the ISBI cell tracking challenge of 2015 (Ronneberger et al. 2015), ConvNet-based methods have become a major focus of attention in medical image analysis fields, such as tumor segmentation (Isensee et al. 2021; Zhou et al. 2019), image reconstruction (Zhu et al. 2018), and disease diagnostics (Lian et al. 2018). In medical image registration, ConvNet-based methods can produce significantly improved registration performance while operating orders of magnitudes faster (after training) compared to traditional methods. ConvNet-based methods replace the costly per-image optimization seen in traditional methods with a single global function optimization during a training phase. The ConvNets learn the common representation of image registration from training images, enabling rapid alignment of an unseen image pair after training. Initially, the supervision of ground-truth deformation fields (which are usually generated using traditional registration methods) is needed for training the neural networks (Onofrey et al. 2013; Yang et al. 2017b; Rohé et al. 2017). Recently, the

*Corresponding author

e-mail: jchen245@jhmi.edu (Junyu Chen), duyong@jhmi.edu (Yong Du), yufanh@nvidia.com (Yufan He), paul.segars@duke.edu (William P. Segars), gary.li@mgh.harvard.edu (Ye Li), efrey@jhmi.edu (Eric C. Frey)

focus has been shifted towards developing unsupervised methods that do not depend on ground-truth deformation fields (Balakrishnan *et al.* 2019; Dalca *et al.* 2019; Kim *et al.* 2021; de Vos *et al.* 2019, 2017; Lei *et al.* 2020; Chen *et al.* 2020; Zhang 2018). Nearly all of the existing deep-learning-based methods mentioned above used U-Net (Ronneberger *et al.* 2015) or the simply modified versions of U-Net (e.g., tweaking the number of layers or changing down- and up-sampling schemes) as their ConvNet designs.

ConvNet architectures generally have limitations in modeling explicit long-range spatial relations (i.e., relations between two voxels that are far away from each other) present in an image due to the intrinsic locality (i.e., the limited effective receptive field) of convolution operations (Luo *et al.* 2016). Even though U-Net (or V-Net (Milletari *et al.* 2016)) was proposed to overcome this limitation by introducing down- and up-sampling operations into a ConvNet, which theoretically enlarges the receptive field of the ConvNet and, thus, encourages the network to consider long-range relationships between points in images. However, several problems remain: first, the receptive fields of the first several layers are still restricted by the convolution-kernel size, and the global information of an image can only be viewed at the deeper layers of the network; second, it has been shown that as the convolutional layers deepen, the impact from far-away voxels decays quickly (Li *et al.* 2021). Therefore, the effective receptive field of a U-Net is, in practice, much smaller than its theoretical receptive field, and it is only a portion of the typical size of a medical image. Yet, it is desirable to have a registration network capable of seeing long-range relationships between points in the moving and fixed images. Otherwise, the network is limited to produce relatively small local deformations, yielding suboptimal registration performance. Many works in other fields (e.g., image segmentation) has addressed this limitation of U-Net (Zhou *et al.* 2019; Jha *et al.* 2019; Devalla *et al.* 2018; Alom *et al.* 2018). To allow for a better flow of multi-scale contextual information throughout the network, Zhou *et al.* (Zhou *et al.* 2019) proposed a nested U-Net (i.e., U-Net++), in which the complex up- and down-samplings along with multiple skip connections were used. Devalla *et al.* (Devalla *et al.* 2018) introduced dilated convolution to the U-Net architecture that enlarges the network's effective receptive field. A similar idea was proposed by Alom *et al.* (Alom *et al.* 2018), where the network's effective receptive field was increased by deploying recurrent convolutional operations. Jha *et al.* proposed ResUNet++ (Jha *et al.* 2019) that incorporates the attention mechanisms into U-Net for modeling long-range spatial information. Despite these methods' promising performance in other medical imaging fields, limited work has been proposed on using advanced network architectures for medical image registration.

Transformer, originated from natural language processing tasks (Vaswani *et al.* 2017), has shown its potential in computer vision tasks. A Transformer deploys self-attention mechanisms to determine which parts of the input sequence (e.g., an image) are essential based on contextual information. Unlike convolution operations, the self-attention mechanisms in a Transformer have unlimited size of the effective receptive field,

making a Transformer capable of capturing long-range spatial information (Li *et al.* 2021). Dosovitskiy *et al.* (Dosovitskiy *et al.* 2020) proposed Vision Transformer (ViT) that applies the Transformer encoder from NLP directly to images. It was the first purely self-attention-based network for computer vision and achieved state-of-the-art performance in image recognition. Subsequent to their success, Swin Transformer (Liu *et al.* 2021a) and its variants (Dai *et al.* 2021; Dong *et al.* 2021) have demonstrated their superior performances in object detection, and semantic segmentation. Recently, Transformer-related methods have gained increased attention in the medical imaging community as well (Chen *et al.* 2021b; Xie *et al.* 2021; Wang *et al.* 2021b; Li *et al.* 2021; Wang *et al.* 2021a; Zhang *et al.* 2021), in which the majority of the methods were applied on the task of image segmentation.

Transformer can be a strong candidate for image registration because it can better comprehend the spatial correspondence between the moving and fixed images. Registration is the process of establishing such correspondence, and intuitively, by comparing different parts of the moving to the fixed image. ConvNet has a narrow field of view and performs convolution locally, limiting its ability to associate the distant parts between two images. For example, if the left part of the moving image matches the right part of the fixed image, ConvNet will be unable to establish the proper spatial correspondence between the two parts if it cannot see both parts concurrently (i.e., when one of the parts falls outside of the ConvNet's field of view). However, Transformer is capable of handling such circumstances and rapidly focusing on the parts that need displacement, owing to its unlimited receptive field and self-attention mechanism.

Our group has previously shown preliminary results that demonstrated the simple bridging of ViT and V-Net could achieve promising performances in image registration (Chen *et al.* 2021a). In this work, we extend the preliminary work and investigate various Transformer models from other tasks (i.e., computer vision and medical imaging tasks) and present a hybrid Transformer-ConvNet framework, TransMorph, for volumetric medical image registration. In this method, the Swin Transformer (Liu *et al.* 2021a) was employed as the encoder to capture the spatial correspondence between the input moving and fixed images. Then, a ConvNet decoder processed the information provided by the Transformer encoder into a dense displacement field. Long skip connections were deployed to maintain the flow of local information between the encoder and decoder stages. We also introduced diffeomorphic variations of TransMorph to ensure a smooth and topology-preserving deformation. Additionally, we applied variational inference on the parameters of TransMorph, resulting in a Bayesian model that predicts registration uncertainty based on the given image pair. Qualitative and quantitative evaluation of the experimental results demonstrate the robustness of the proposed method and confirm the efficacy of Transformers for image registration.

The main contributions of this work are summarized as follows:

- *Transformer-based model:* This paper presents the pioneering work on using Transformers for image registration. A novel Transformer-based neural network,

TransMorph, was proposed for affine and deformable image registration.

- **Architecture analysis:** Experiments in this paper demonstrate that positional embedding, which is a commonly used element in Transformer by convention, is not required for the proposed hybrid Transformer-ConvNet model. Additionally, this paper provides proof that Transformer-based models have larger effective receptive fields than ConvNets.
- **Diffeomorphic registration:** Two diffeomorphic variants of TransMorph are presented that ensure a diffeomorphism in the deformation.
- **Uncertainty quantification:** This paper also provides a Bayesian uncertainty variant of TransMorph that yields perfectly calibrated uncertainty estimates.
- **State-of-the-art results:** We extensively validate the proposed registration models on the brain MRI registration application and on a novel application of XCAT-to-CT registration with an aim to create a population of anatomically variable XCAT phantom. The datasets used in this study include over 1000 image pairs for training and testing. The proposed models were compared with various registration methods and demonstrated state-of-the-art performance. **Eight** registration approaches were employed as baselines, including learning-based methods and commonly used traditional methods. The performances of **four** recently proposed Transformer architectures from other tasks (e.g., semantic segmentation, classification, etc.) were also evaluated on the task of image registration.
- **Open source:** We provide the community with a fast and accurate tool for deformable registration. The code and the trained model is publicly available at <https://bit.ly/37eJS6N>.

The paper is organized as follows. Section 2 discusses the related works. Section 3 explains the proposed methodology. Section 4 discusses experimental setup, implementation details, and datasets used in this study. Section 5 presents experimental results. Section 6 discusses the findings based on the results, and Section 7 concludes the paper.

2. Related Work

2.1. Image Registration

DIR establishes spatial correspondence between two images by optimizing an energy function:

$$E(I_m, I_f, \phi) = E_{sim}(I_m \circ \phi, I_f) + \lambda R(\phi), \quad (1)$$

where I_m and I_f denote, respectively, the moving and fixed image, ϕ denotes the deformation field that warps the moving image (i.e., $I_m \circ \phi$), $R(\phi)$ imposes smoothness of the deformation field, and λ is the regularization trade-off parameter. The optimal warping, $\hat{\phi}$ is given by minimizing this energy function:

$$\hat{\phi} = \arg \min_{\phi} E(I_m, I_f, \phi). \quad (2)$$

In the energy function, E_{sim} measures the level of alignment between the deformed moving image, $I_m \circ \phi$, and the fixed image, I_f . Some common choices for E_{sim} are mean squared error (MSE) (Beg et al. 2005), sum of squared differences (SSD) (Wolberg and Zokai 2000), normalized cross-correlation (NCC) (Avants et al. 2008), structural similarity index (SSIM) (Chen et al. 2020), and mutual information (MI) (Viola and Wells III 1997). The regularization term, $R(\phi)$, imposes spatial smoothness on the deformation field. A common assumption in most applications is that similar structures exist in both moving and fixed images. As a result, a continuous and invertible deformation field (i.e., a diffeomorphism) is needed to preserve topology, and the regularization, $R(\phi)$ is meant to enforce or encourage this. Isotropic diffusion (equivalent to Gaussian smoothing) (Balakrishnan et al. 2019), anisotropic diffusion (Pace et al. 2013), total variation (Vishnevskiy et al. 2016), and bending energy (Johnson and Christensen 2002) are the popular options for $R(\phi)$.

2.1.1. Image registration via deep neural networks

While traditional image registration methods iteratively minimize the energy function in (1) for each pair of moving and fixed images, DNN-based methods optimize the energy function for a training dataset, thereby learning a global representation of image registration that enables alignment of an unseen pair of volumes. DNN methods are often categorized as supervised or unsupervised, with the former requiring a ground truth deformation field for training and the latter relying only on the image datasets.

In supervised DNN methods, the ground-truth deformation fields are either produced synthetically or generated by the traditional registration methods (Yang et al. 2017b; Sokooti et al. 2017; Cao et al. 2018). Yang et al. 2017b proposed a supervised ConvNet that predicts the LDDMM (Beg et al. 2005) momentum from image patches. Sokooti et al. 2017 trained a registration ConvNet with synthetic displacement fields. The ground-truth deformation fields are often computationally expensive to generate, and the registration accuracy of these methods is highly dependent on the quality of the ground truth.

Due to the limitations of supervised methods, the focus of research has switched to unsupervised DNN methods that do not need ground-truth deformation fields. Unsupervised DNNs optimize an energy function on the input images, similarly to traditional methods. However, DNN-based methods learn a common registration representation from a training set and then apply it to unseen images. Note that the term "unsupervised" refers to the absence of ground-truth deformation fields, but the network still needs training (this is also known as "self-supervised"). de Vos et al. 2019; Balakrishnan et al. 2018, 2019 are the representative ones of unsupervised DNN-based methods.

Later on, diffeomorphic deformation representation was developed to address the issue of non-smooth deformations in DNN-based methods. We briefly introduce its concepts in the next subsection.

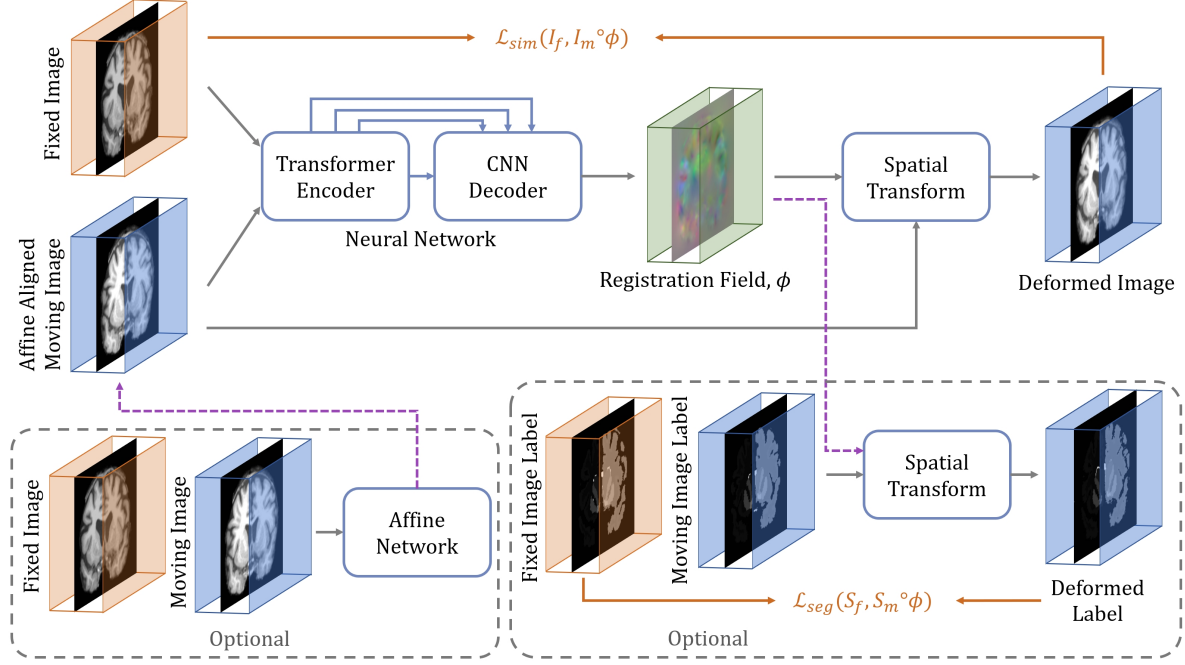


Fig. 1. The overall framework of the proposed Transformer-based image registration model, TransMorph.

2.1.2. Diffeomorphism via deep neural networks

Diffeomorphic deformable image registration is important in many medical image applications, owing to its special properties including topology preservation and transformation invertibility. A diffeomorphism is a smooth and continuous one-to-one mapping with invertible derivatives (i.e., non-zero Jacobian determinant). In some traditional methods (e.g., LDDMM (Beg et al. 2005) and SyN (Avants et al. 2008)), a diffeomorphic deformation field ϕ can be obtained via the time-integration of a time-varying velocity field $v^{(t)}$, i.e., $\frac{d}{dt}\phi^{(t)} = v^{(t)}(\phi^{(t)})$, where $\phi^{(t)} = id$ is the identity transform. On the other hand, learning-based diffeomorphic models (Dalca et al. 2019; Mok and Chung 2020; Shen et al. 2019; Niethammer et al. 2019; Krebs et al. 2019) primarily use stationary velocity field (SVF) with an efficient scaling-and-squaring approach (Arsigny et al. 2006), because it can be implemented with relative ease. In the scaling-and-squaring approach, the deformation field is represented as a Lie algebra member that is exponentiated to generate a time 1 deformation $\phi^{(1)}$, which is a member of the Lie group: $\phi^{(1)} = \exp(v)$. This means that the exponentiated flow field compels the mapping to be diffeomorphic and invertible using the same flow field. Starting from an initial deformation field:

$$\phi^{(1/2^T)} = p + \frac{v(p)}{2^T}, \quad (3)$$

where p denotes the spatial locations. The $\phi^{(1)}$ can be obtained using the recurrence:

$$\phi^{(1/2^{t-1})} = \phi^{(1/2^t)} \circ \phi^{(1/2^t)}. \quad (4)$$

Thus, $\phi^{(1)} = \phi^{(1/2)} \circ \phi^{(1/2)}$.

In practice, a neural network first generates a displacement field, which is then scaled by $1/2^T$ to produce an initial deformation field $\phi^{(1/2^T)}$. Subsequently, the squaring technique

(i.e., Eqn. 4) is applied recursively to $\phi^{(1/2^T)}$ T times via a spatial transformation function, resulting in a final diffeomorphic deformation field $\phi^{(1)}$. Despite the fact that diffeomorphisms are theoretically guaranteed to be invertible, interpolation errors can lead to invertibility errors that rise linearly with the number of interpolation steps (Avants et al. 2008; Mok and Chung 2020).

2.2. Self-attention Mechanism and Transformer

Transformer makes use of the self-attention mechanism that estimates the relevance of one input sequence to another via the Query-Key-Value (QKV) model (Vaswani et al. 2017; Dosovitskiy et al. 2020). The input sequences are often originated from the flattened patches of an image. Let \mathbf{x} be an image volume defined over a 3D spatial domain (i.e., $\mathbf{x} \in \mathbb{R}^{H \times W \times L}$). The image is first divided into N flattened 3D patches $\mathbf{x}_p \in \mathbb{R}^{N \times P^3}$, where (H, W, L) is the size of the original image, (P, P, P) is the size of each image patch, and $N = \frac{HWL}{P^3}$. Then, a learnable linear embedding \mathbf{E} is applied to \mathbf{x}_p , which projects each patch into a $D \times 1$ vector representation:

$$\hat{\mathbf{x}}_e = [\mathbf{x}_p^1 \mathbf{E}; \mathbf{x}_p^2 \mathbf{E}; \dots; \mathbf{x}_p^N \mathbf{E}], \quad \mathbf{E} \in \mathbb{R}^{P^3 \times D} \quad (5)$$

Then, a learnable positional embedding is added to $\hat{\mathbf{x}}_e$ so that the patches can retain their positional information, i.e., $\mathbf{x}_e = \hat{\mathbf{x}}_e + \mathbf{E}_{pos}$, where $\mathbf{E}_{pos} \in \mathbb{R}^{N \times D}$. These vector representations, often known as tokens, are subsequently used as inputs for self-attention computations.

Self-attention. To compute self-attention (SA), $\mathbf{x}_e \in \mathbb{R}^{N \times D}$ is encoded by \mathbf{U} to three matrix representations: queries $\mathbf{Q} \in \mathbb{R}^{N \times D_k}$, keys $\mathbf{K} \in \mathbb{R}^{N \times D_k}$, and values $\mathbf{V} \in \mathbb{R}^{N \times D_v}$. The scaled

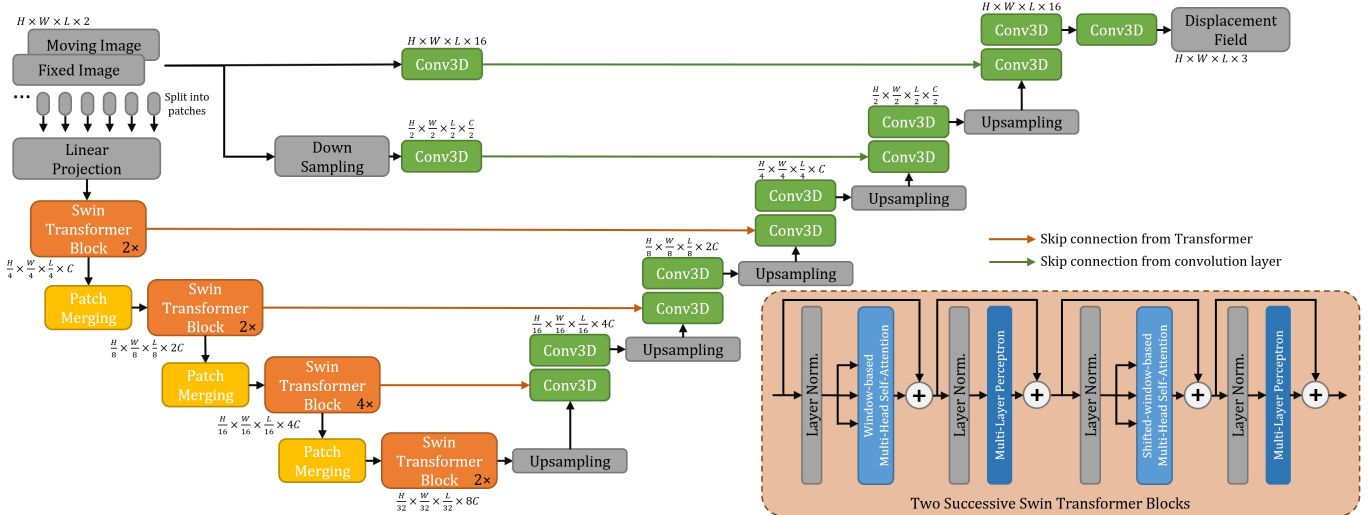


Fig. 2. The architecture of the proposed TransMorph registration network.

dot-product attention is given by:

$$\begin{aligned} [\mathbf{Q}, \mathbf{K}, \mathbf{V}] &= \mathbf{x}_e \mathbf{U}_{q,k,v} \quad \mathbf{U}_{q,k,v} \in \mathbb{R}^{D \times D_{q,k,v}}, \\ \mathbf{A} &= \text{softmax}(\frac{\mathbf{Q}\mathbf{K}^\top}{\sqrt{D_k}}) \quad \mathbf{A} \in \mathbb{R}^{N \times N}, \\ SA(\mathbf{x}_e) &= \mathbf{A}\mathbf{V}, \end{aligned} \quad (6)$$

where \mathbf{A} is the attention weight matrix, each element of \mathbf{A} represents the pairwise similarity between two elements of the input sequence \mathbf{x}_e and their respective query and key representations.

Multi-head self-attention. A Transformer employs multi-head self-attention (MSA) rather than a single attention function. MSA is an extension of self-attention in which h self-attention operations (i.e., "heads") are processed simultaneously, then their outputs are concatenated then projected onto a D -dimensional representation:

$$MSA(\mathbf{x}_e) = [SA_1(\mathbf{x}_e); SA_2(\mathbf{x}_e); \dots; SA_h(\mathbf{x}_e)] \mathbf{U}_{MSA}, \quad (7)$$

where $\mathbf{U}_{MSA} \in \mathbb{R}^{h \cdot D_h \times D}$, and D_h is typically set to D/h in order to keep the number of parameters constant before and after the MSA operation.

2.3. Bayesian Deep Learning

Uncertainty estimates help comprehend what a machine learning model does not know. They indicate the likelihood that a neural network may make an incorrect prediction. Because most deep neural networks are incapable of representing uncertainty, their predictions are frequently taken at face value and thought to be correct. *Bayesian deep learning* estimates predictive uncertainty, providing a realistic paradigm for understanding uncertainty within deep neural networks (Gal and Ghahramani 2016). The uncertainty caused by the parameters in a neural network is known as epistemic uncertainty, which is modeled by placing a prior distribution (e.g., a Gaussian prior distribution: $\mathbf{W} \sim \mathcal{N}(0, I)$) on the parameters of a network and then attempting to capture how much these weights

vary given specific data. Recent efforts in this area include the *Bayes by Backprop* (Blundell et al. 2015), its closely related mean-field variational inference by assuming a Gaussian prior distribution (Tölle et al. 2021), stochastic batch normalization (Atanov et al. 2018), and Monte-Carlo (MC) dropout (Gal and Ghahramani 2016; Kendall and Gal 2017). The applications of Bayesian deep learning in medical imaging expands on image denoising (Tölle et al. 2021; Laves et al. 2020b) and image segmentation (DeVries and Taylor 2018; Baumgartner et al. 2019; Mehrtash et al. 2020). In deep-learning-based image registration, the majority of methods provide a single, deterministic solution of the unknown geometric transformation. Knowing about epistemic uncertainty helps determine if and to what degree the registration results can be trusted and whether the input data is appropriate for the neural network. The registration uncertainty estimations may be used for uncertainty-weighted registration (Simpson et al. 2011; Kybic 2009), surgical treatment planning, or directly visualized for qualitative evaluations (Yang et al. 2017b). Cui et al. (Cui et al. 2021) and Yang et al. (Yang et al. 2017b) incorporated MC dropout layers in the registration network design, which allows for uncertainty estimates by sampling multiple deformation field predictions from the network.

The proposed image registration framework expands on these ideas. In particular, a new registration framework is presented, which uses Transformer for network design, diffeomorphism for image registration, and Bayesian deep learning to estimate registration uncertainty.

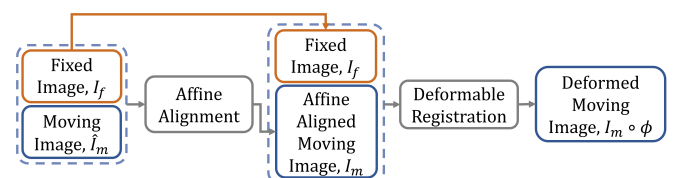


Fig. 3. The conventional paradigm of image registration.

3. Methods

The conventional paradigm of image registration is shown in Fig. 3. The moving and fixed images, denoted respectively as \hat{I}_m and I_f , are first affinely transformed into a single coordinate system. The resulting affine-aligned moving image is denoted as I_m . Subsequently, I_m is warped to I_f using a deformation field, ϕ , generated by a DIR algorithm (i.e., $I_m \circ \phi$). Fig. 1 presents an overview of the proposed method. Here, both the affine transformation and the deformable registration are performed using Transformer-based neural networks. The affine Transformer takes \hat{I}_m and I_f as inputs and computes a set of affine transformation parameters (e.g., rotation angle, translation, etc.). These parameters are used to affinely align \hat{I}_m with I_f via an affine transformation function, yielding an aligned image I_m . Then, a DIR network computes a deformation field ϕ given I_m and I_f , which warps I_m using a spatial transformation function (i.e., $\hat{I}_f = I_m \circ \phi$). During training, the DIR network may optionally leverage supplementary information (e.g., anatomical segmentations). The network architectures, the loss and regularization functions, and the variants of the method are described in detail in the following sections.

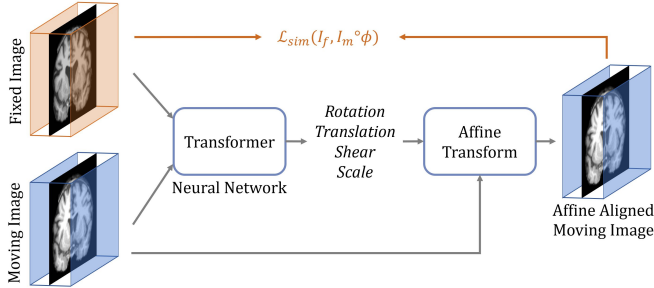


Fig. 4. The framework of the proposed Transformer-based affine model.

3.1. Affine Transformation Network

Affine transformation is often used as the initial stage in image registration because it facilitates the optimization of the following more complicated DIR processes (de Vos et al. 2019). An affine network examines a pair of moving and fixed images globally and produces a set of transformation parameters that aligns the moving image with the fixed image. Here, the architecture of the proposed Transformer-based affine network is a modified Swin Transformer (Liu et al. 2021a) that takes two 3D volumes as the inputs (i.e., I_f and \hat{I}_m) and generates 12 affine parameters: three rotation angles, three translation parameters, three scaling parameters, and three shearing parameters. The details and a visualization of the architecture are shown in Fig. A.18 in the Appendix. We reduced the number of parameters in the original Swin Transformer due to the relative simplicity of affine registration. The specifics of the Transformer's architecture and parameter settings are covered in a subsequent section.

3.2. Deformable Registration Network

Fig. 2 shows the network architecture of the proposed TransMorph. The encoder of the network first splits the input

moving and fixed volumes into non-overlapping 3D patches, each of size $2 \times P \times P \times P$, where P is typically set to 4 (Dosovitskiy et al. 2020; Liu et al. 2021a; Dong et al. 2021). We denote the i^{th} patch as x_p^i , where $i \in \{1, \dots, N\}$ and $N = \frac{H}{P} \times \frac{W}{P} \times \frac{L}{P}$ is the total number of patches. Each patch is flattened and regarded as a "token", and then a linear projection layer is used to project each token to a feature representation of an arbitrary dimension (denoted as C):

$$\mathbf{z}_0 = [x_p^1 \mathbf{E}; x_p^2 \mathbf{E}; \dots; x_p^N \mathbf{E}], \quad (8)$$

where $\mathbf{E} \in \mathbb{R}^{2P^3 \times C}$ denotes the linear projection, and the output \mathbf{z}_0 has a dimension of $N \times C$.

Because the linear projection operates on image patches and does not keep the token's location relative to the image as a whole, existing Transformers often add a positional embedding to the linear projections in order to integrate the positional information into tokens, i.e. $\mathbf{z}_0 + \mathbf{E}_{pos}$ (Vaswani et al. 2017; Dosovitskiy et al. 2020; Liu et al. 2021a; Dong et al. 2021). Such Transformers were primarily designed for image classification, where the output is often a vector describing the likelihood of an input image being classified as a certain class. Thus, if the positional embedding is not employed, the Transformer may lose the positional information. However, for pixel-level tasks such as image registration, the network often includes a decoder that generates a dense prediction with the same resolution as the input or target image. The exact voxel locations in the output image is enforced by comparing the output with the target image using a loss function. Any spatial mismatches between output and target would contribute to the loss and be backpropagated into the Transformer encoder. The Transformer should thereby inherently capture the tokens' positional information. In this work, we observed that positional embedding is not necessary for image registration, and it only adds extra parameters to the network without improving performance. The effects of positional embedding will be discussed in more detail later in this paper.

Following the linear projection layer, several consecutive stages of patch merging and Swin Transformer blocks (Liu et al. 2021a) are applied on the tokens \mathbf{z}_0 . The Swin Transformer blocks outputs the same number of tokens as the input, while the patch merging layers concatenate the features of each group of $2 \times 2 \times 2$ neighboring tokens, thus they reduce the number of tokens by a factor of $2 \times 2 \times 2 = 8$ (e.g., $\frac{H}{4} \times \frac{W}{4} \times \frac{L}{4} \times C \rightarrow \frac{H}{8} \times \frac{W}{8} \times \frac{L}{8} \times 8C$). Then, a linear layer is applied on the $8C$ -dimensional concatenated features to produce features each of $2C$ -dimension. After four stages of Swin Transformer blocks and three stages of patch merging in between the Transformer stages (i.e., orange boxes in Fig. 2), the output dimension at the last stage of the encoder is $\frac{H}{32} \times \frac{W}{32} \times \frac{L}{32} \times 8C$. The decoder consists of successive upsampling and convolutional layers with the kernel size of 3×3 . Each of the upsampled feature maps in the decoding stage was concatenated with the corresponding feature map from the encoding path via skip connections, then followed by two consecutive convolutional layers. As shown in Fig. 2, the Transformer encoder can only provide feature maps up to a resolution of $\frac{H}{P} \times \frac{W}{P} \times \frac{L}{P}$ owing to the nature of patch operation (denoted by the orange arrows).

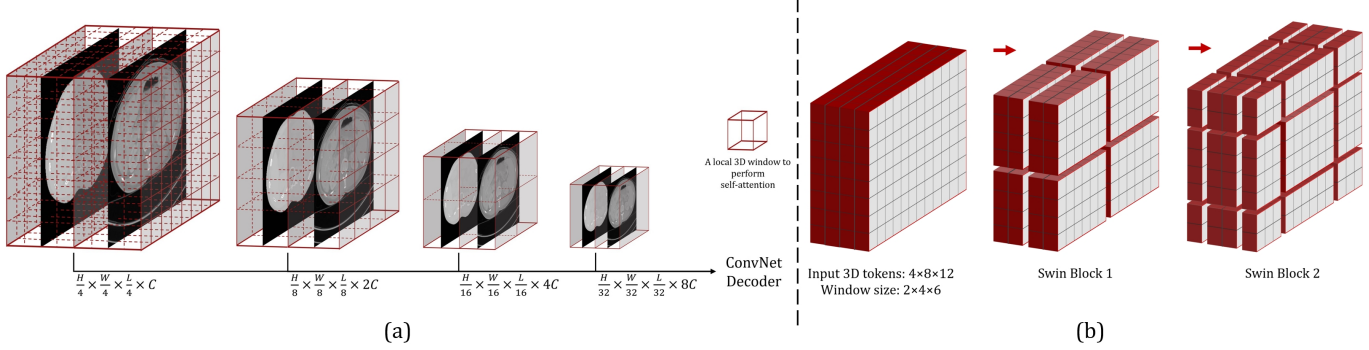


Fig. 5. (a): Swin Transformer creates hierarchical feature maps by merging image patches. The self-attention is computed within each local 3D window (the red box). The feature maps generated at each resolution are sent into a ConvNet decoder to produce an output. (b): The 3D cyclic shift of local windows for shifted-window-based self-attention computation.

Hence, Transformer may fall short of delivering high-resolution feature maps and aggregating local information at lower layers (Raghu et al. 2021). To address this shortcoming, we employed two convolutional layers using the original and downsampled image pair as inputs to capture local information and generate high-resolution feature maps. The outputs of these layers were concatenated with the feature maps in the decoder to produce a deformation field. The final deformation field, ϕ , was generated by applying sixteen 3×3 convolutions. Except for the last convolutional layer, each convolutional layer is followed by a Leaky Rectified Linear Unit (Maas et al. 2013) activation.

In the next subsections, we discuss the Swin Transformer block, the spatial transformation function, and the loss functions in detail.

3.2.1. 3D Swin Transformer Block

Swin Transformer (Liu et al. 2021a) can generate hierarchical feature maps at various resolutions by using patch merging layers, making it ideal for usage as a general-purpose backbone for pixel-level tasks like image registration and segmentation. Swin Transformer’s most significant component, apart from patch merging layers, is the shifted window-based self-attention mechanism. Unlike ViT (Dosovitskiy et al. 2020), which computes the relationships between a token and all other tokens at each step of the self-attention modules. Swin Transformer computes self-attention within the evenly partitioned non-overlapping local windows of the original and the lower resolution feature maps (as shown in Fig. 5 (a)). In contrast to the original Swin Transformer, this work uses rectangular-shaped windows to accommodate non-square images, and each has a shape of $M_x \times M_y \times M_z$. At each resolution, the first Swin Transformer block employs a regular window partitioning method, beginning with the top-left voxel, and the feature maps are evenly partitioned into non-overlapping windows of size $M_x \times M_y \times M_z$. The self-attention is then calculated locally within each window. To introduce connections between neighboring windows, Swin Transformer uses a shifted window design, i.e., in the successive Swin Transformer blocks, the windowing configuration shifts from that of the preceding block, by displacing the windows in the preceding block by $(\lfloor \frac{M_x}{2} \rfloor \times \lfloor \frac{M_y}{2} \rfloor \times \lfloor \frac{M_z}{2} \rfloor)$ voxels. As illustrated by an example in

Fig. 5 (b), the input feature map has $4 \times 8 \times 12$ voxels. With a window size of $2 \times 4 \times 6$, the feature map is evenly partitioned into $2 \times 2 \times 2$ number of windows in the first Swin Transformer block (“Swin Block 1” in Fig. 5 (b)). Then, in the next block, the windows are shifted by $(\lfloor \frac{2}{2} \rfloor \times \lfloor \frac{4}{2} \rfloor \times \lfloor \frac{6}{2} \rfloor) = (1 \times 2 \times 3)$, and the number of windows becomes $3 \times 3 \times 3 = 27$. We extended the original 2D efficient batch computation (i.e., cyclic shift) (Liu et al. 2021a,b) to 3D and applied it to the 27 shifted windows, keeping the final number of windows for attention computation at 8. With the windowing-based attention, two consecutive Swin Transformer blocks can be computed as:

$$\begin{aligned} \hat{\mathbf{z}}_\ell &= \text{W-MSA}(\text{LN}(\mathbf{z}_{\ell-1})) + \mathbf{z}_{\ell-1}, \\ \mathbf{z}_\ell &= \text{MLP}(\text{LN}(\hat{\mathbf{z}}_\ell)) + \hat{\mathbf{z}}_\ell, \\ \hat{\mathbf{z}}_{\ell+1} &= \text{SW-MSA}(\text{LN}(\mathbf{z}_\ell)) + \mathbf{z}_\ell, \\ \mathbf{z}_{\ell+1} &= \text{MLP}(\text{LN}(\hat{\mathbf{z}}_{\ell+1})) + \hat{\mathbf{z}}_{\ell+1}, \end{aligned} \quad (9)$$

where W-MSA and SW-MSA stand for, respectively, window-based multi-head self-attention and shifted-window-based multi-head self-attention module; MLP denotes the multi-layer perceptron module (Vaswani et al. 2017); $\hat{\mathbf{z}}_\ell$ and \mathbf{z}_ℓ denote the output features of the (S)W-MSA and the MLP module for block ℓ , respectively. The self-attention is computed as:

$$\mathbf{A}(Q, K, V) = \text{softmax}(\frac{QK^\top}{\sqrt{d}} + B)V, \quad (10)$$

where $Q, K, V \in \mathbb{R}^{M_x M_y M_z \times d}$ are *query*, *key*, *value* matrices, d denotes the dimension of *query* and *key* features, $M_x M_y M_z$ is the number of tokens in a 3D window, and B represents the relative position of tokens in each window. Since the relative position between tokens along each axis (i.e., x, y, z) can only take values from $[-M_{x,y,z} + 1, M_{x,y,z} - 1]$, the values in B are taken from a smaller bias matrix $\hat{B} \in \mathbb{R}^{(2M_x-1) \times (2M_y-1) \times (2M_z-1)}$.

3.2.2. Spatial Transformation Function

The spatial transformation function proposed in (Jaderberg et al. 2015) is used to apply a nonlinear warp to the moving image I_m with the deformation field ϕ (or the displacement field \mathbf{u}) provided by the network. The intensity of each voxel location \mathbf{p} in the output image is determined by:

$$I_m \circ \phi(\mathbf{p}) = I_m(\mathbf{p} - \mathbf{u}(\mathbf{p})). \quad (11)$$

Note that $\mathbf{p} - \mathbf{u}(\mathbf{p})$ is not necessarily an integer, and voxel intensities are only defined at integer locations in an image. Thus, the intensity at $I_m \circ \phi(\mathbf{p})$ is obtained by applying interpolation methods to the intensities of the neighboring voxels around $\mathbf{p} - \mathbf{u}(\mathbf{p})$:

$$I_m \circ \phi(\mathbf{p}) = \sum_{\mathbf{q} \in \mathcal{Z}(\hat{\mathbf{p}})} I_m(\mathbf{q}) \prod_{d \in \{x,y,z\}} k(\hat{\mathbf{p}}_d - \mathbf{q}_d), \quad (12)$$

where $\hat{\mathbf{p}} = \mathbf{p} - \mathbf{u}(\mathbf{p})$, $\mathcal{Z}(\hat{\mathbf{p}})$ denotes the neighboring voxel locations of $\hat{\mathbf{p}}$, d denotes the three directions in 3D image space, and $k(\cdot)$ is a generic sampling kernel that defines the interpolation method (e.g., tri-linear, nearest-neighbor, etc.). Tri-linear interpolation is often used on images, while nearest-neighbor is often used on label maps. Due to the non-differentiable nature of the nearest-neighbor sampling kernel, it can only be used for inference and not for network training.

3.2.3. Loss Functions

The overall loss function for network training derives from the energy function of the traditional image registration algorithms (i.e., Eqn. (1)). The loss function consists of two parts: one computes the similarity between the deformed moving and the fixed images, and another one regularizes the deformation field so that it is smooth:

$$\mathcal{L}(I_f, I_m, \phi) = \mathcal{L}_{sim}(I_f, I_m, \phi) + \lambda \mathcal{R}(\phi), \quad (13)$$

where \mathcal{L}_{sim} denotes the image fidelity measure, and \mathcal{R} denotes the deformation field regularization.

Image Similarity Measure. In this work, we experimented with two widely-used similarity metric for \mathcal{L}_{sim} . The first is the mean squared error, which is the mean of the squared difference in voxel values between I_f and I_m :

$$MSE(I_f, I_m, \phi) = \frac{1}{\Omega} \sum_{\mathbf{p} \in \Omega} |I_f(\mathbf{p}) - [I_m \circ \phi](\mathbf{p})|^2, \quad (14)$$

where \mathbf{p} denotes the voxel location, and Ω represents the image domain.

Another similarity metric is the local normalized cross-correlation between I_f and I_m :

$$LNCC(I_f, I_m, \phi) = \sum_{\mathbf{p} \in \Omega} \frac{\left(\sum_{\mathbf{p}_i} (f(\mathbf{p}_i) - \bar{f}(\mathbf{p}))([I_m \circ \phi](\mathbf{p}_i) - [\bar{I}_m \circ \phi](\mathbf{p})) \right)^2}{\left(\sum_{\mathbf{p}_i} (f(\mathbf{p}_i) - \bar{f}(\mathbf{p}))^2 \right) \left(\sum_{\mathbf{p}_i} ([I_m \circ \phi](\mathbf{p}_i) - [\bar{I}_m \circ \phi](\mathbf{p}))^2 \right)}, \quad (15)$$

where $\bar{I}_f(\mathbf{p})$ and $\bar{I}_m(\mathbf{p})$ denotes the mean voxel value within the local window of size n^3 centered at voxel \mathbf{p} , and $n = 9$ in our experiments.

Deformation Field Regularization. Optimizing the similarity metric solely would encourage $I_m \circ \phi$ to be visually as close as possible to I_f . The resulting deformation field ϕ , however, might not be smooth or realistic. To impose smoothness in the deformation field, a regularizer $\mathcal{R}(\phi)$ is added to the loss function. $\mathcal{R}(\phi)$ encourages the displacement value in a location to

be similar to the values in its neighboring locations. Here, we experimented with two regularizers for $\mathcal{R}(\phi)$. The first is the diffusion regularizer [Balakrishnan et al. 2019](#):

$$\mathcal{R}_{diffusion}(\phi) = \sum_{\mathbf{p} \in \Omega} \|\nabla \mathbf{u}(\mathbf{p})\|^2, \quad (16)$$

where $\mathbf{u}(\mathbf{p})$ is the spatial gradients of the displacement field \mathbf{u} . The spatial gradients are approximated using forward differences, that is, $\frac{\partial \mathbf{u}(\mathbf{p})}{\partial (x,y,z)} \approx \mathbf{u}(p_{\{x,y,z\}} + 1) - \mathbf{u}(p_{\{x,y,z\}})$.

The second regularizer is bending energy [Rueckert et al. 1999](#), which penalizes sharply curved deformations, thus, it may be helpful for abdominal organ registration. Bending energy operates on the second derivative of the displacement field \mathbf{u} , and it is defined as:

$$\mathcal{R}_{bending}(\phi) = \sum_{\mathbf{p} \in \Omega} \|\nabla^2 \mathbf{u}(\mathbf{p})\|^2 = \sum_{\mathbf{p} \in \Omega} \left[\left(\frac{\partial^2 \mathbf{u}(\mathbf{p})}{\partial x^2} \right)^2 + \left(\frac{\partial^2 \mathbf{u}(\mathbf{p})}{\partial y^2} \right)^2 + \left(\frac{\partial^2 \mathbf{u}(\mathbf{p})}{\partial z^2} \right)^2 + 2 \left(\frac{\partial^2 \mathbf{u}(\mathbf{p})}{\partial xz} \right)^2 + 2 \left(\frac{\partial^2 \mathbf{u}(\mathbf{p})}{\partial xy} \right)^2 + 2 \left(\frac{\partial^2 \mathbf{u}(\mathbf{p})}{\partial yz} \right)^2 \right], \quad (17)$$

where the derivatives are estimated using the same forward differences that were used previously.

Auxiliary Segmentation Information. When the organ segmentation of I_f and I_m is available, TransMorph may leverage this auxiliary information during training for improving the anatomical mapping between $I_m \circ \phi$ and I_f . A loss function \mathcal{L}_{seg} that quantifies the segmentation overlap is added to the overall loss function (Eqn. 13):

$$\mathcal{L}(I_f, I_m, \phi) = \mathcal{L}_{sim}(I_f, I_m, \phi) + \lambda \mathcal{R}(\phi) + \gamma \mathcal{L}_{seg}(s_f, s_m, \phi), \quad (18)$$

where s_f and s_m represent, respectively, the organ segmentation of I_f and I_m , and γ is a weighting parameter that controls the strength of \mathcal{L}_{seg} . In the field of image registration, it is common to use Dice score [Dice 1945](#) as a figure of merit to quantify registration performance. Therefore, we directly minimized the Dice loss [Milletari et al. 2016](#) between s_f^k and s_m^k , where k represents the k^{th} structure/organ:

$$Dice(s_f, s_m, \phi) = 1 - \frac{1}{K} \sum_k \frac{2 \sum_{\mathbf{p} \in \Omega} s_f^k(\mathbf{p}) [s_m^k \circ \phi](\mathbf{p})}{\sum_{\mathbf{p} \in \Omega} (s_f^k(\mathbf{p}))^2 + \sum_{\mathbf{p} \in \Omega} (s_m^k \circ \phi)(\mathbf{p})^2}. \quad (19)$$

$s_m \circ \phi$ should ideally be implemented via nearest-neighbor interpolation, since s_m^k is a binary mask. As mentioned in Section 3.2.2, nearest-neighbor interpolation is not differentiable, and therefore cannot be used for network training. Here, we used a method similar to that described in [Balakrishnan et al. 2019](#), in which we designed s_f and s_m as image volumes with K channels, each channel containing a binary mask defining the segmentation of a specific structure/organ. Then, $s_m \circ \phi$ is computed by warping the K -channel s_m with ϕ using linear interpolation so that the gradients of \mathcal{L}_{seg} can be backpropagated into the network.

3.3. Diffeomorphic Variants

In this section, we present two variants of TransMorph that guarantee a diffeomorphic deformation such that the resulting deformable mapping is continuous, differentiable, and preserves topology. We achieved diffeomorphic registration using the *scaling-and-squaring* approach (described in section 2.1.2) with a stationary velocity field representation (Arsigny et al. 2006). The two existing diffeomorphic models, VoxelMorph-diff (Dalca et al. 2019) and MIDIR (Qiu et al. 2021), have been adopted as bases for the proposed TransMorph diffeomorphic variants, designated by TransMorph-diff (section 3.3.1) and TransMorph-bspl (section 3.3.2), respectively. The next subsections discuss these models in depth.

3.3.1. Probabilistic diffeomorphic registration

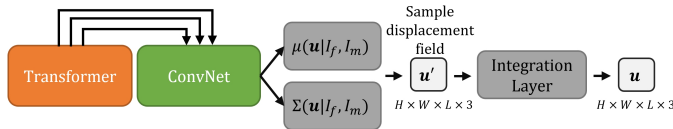


Fig. 6. The architecture of the probabilistic diffeomorphic TransMorph.

As shown in Fig. 6, we introduced a variational inference framework to the proposed TransMorph (which we denote as TransMorph-diff.). A prior distribution

$$p(\mathbf{u}) = \mathcal{N}(\mathbf{u}; \mathbf{0}, \Sigma_{\mathbf{u}}) \quad (20)$$

was placed over the dense displacement field \mathbf{u} , where $\mathbf{0}$ and $\Sigma_{\mathbf{u}}$ are the mean and covariance of the multivariate normal distribution. We followed (Dalca et al. 2019) and defined $\Sigma_{\mathbf{u}}^{-1} = \Lambda_{\mathbf{u}} = \lambda \mathbf{L}$, where $\Lambda_{\mathbf{u}}$ denotes the precision matrix, λ controls the scale of \mathbf{u} , $\mathbf{L} = \mathbf{D} - \mathbf{A}$ is the Laplacian matrix of a neighborhood graph formed on the voxel grid, \mathbf{D} is the graph degree matrix, and \mathbf{A} is a voxel neighborhood adjacency matrix. The probability $p(I_f|I_m)$ can be computed using the law of total probability:

$$p(I_f|I_m) = \int p(I_f|\mathbf{u}, I_m) p(\mathbf{u}) d\mathbf{u}. \quad (21)$$

The likelihood $p(I_f|\mathbf{u}, I_m)$ was also assumed to be Gaussian

$$p(I_f|\mathbf{u}, I_m) = \mathcal{N}(I_f; I_m \circ \phi_{\mathbf{u}}, \sigma_{\mathbf{I}}^2 \mathbb{I}), \quad (22)$$

where $\sigma_{\mathbf{I}}^2$ captures the variance of the image noise, and $\phi_{\mathbf{u}}$ is the group exponential of the time-stationary velocity field \mathbf{u} , i.e. $\phi = \exp(\mathbf{u})$, which is computed using the *scaling-and-squaring* approach (section 2.1.2).

Our goal is to estimate the posterior probability $p(\mathbf{u}|I_f, I_m)$. Due to the intractable nature of the integral over \mathbf{u} in Eqn. 21, $p(I_f|I_m)$ is usually calculated using just the \mathbf{u} 's that are most likely to have generated I_f (Krebs et al. 2019). Since computing the posterior $p(\mathbf{u}|I_f, I_m)$ analytically is also intractable, we instead assumed a variational posterior $q_{\psi}(\mathbf{u}|I_f, I_m)$ learned by the network with parameters ψ . The Kullback-Leibler divergence (KL) is used to relate the variational posterior to the actual posterior, which results in the evidence lower limit (ELBO)

(Kingma and Welling 2013):

$$\log p(I_f|I_m) - \text{KL} \left[q_{\psi}(\mathbf{u}|I_f, I_m) \parallel p(\mathbf{u}|I_f, I_m) \right] = \mathbb{E}_{\mathbf{u} \sim q_{\psi}} \left[\log p(I_f|\mathbf{u}, I_m) \right] - \text{KL} \left[q_{\psi}(\mathbf{u}|I_f, I_m) \parallel p(\mathbf{u}) \right], \quad (23)$$

where the KL-divergence on the left hand side vanishes if the variational posterior is identical to the actual posterior. Therefore, maximizing $\log p(I_f|I_m)$ is equivalent to minimizing the negative of ELBO on the right hand side of Eqn. 23. Since the prior distribution $p(\mathbf{u})$ was assumed to be a multivariate Gaussian, the variational posterior is likewise a multivariate Gaussian, defined as:

$$q_{\psi}(\mathbf{u}|I_f, I_m) = \mathcal{N}(\mathbf{u}; \mu_{\psi}(\mathbf{u}|I_f, I_m), \Sigma_{\psi}(\mathbf{u}|I_f, I_m)), \quad (24)$$

where μ_{ψ} and Σ_{ψ} are the voxel-wise mean and variance generated by the network with parameters ψ . In each forward pass, the dense displacement field \mathbf{u} is sampled using reparameterization $\mathbf{u} = \mu_{\psi} + \Sigma_{\psi} \odot \epsilon$ with $\epsilon \sim \mathcal{N}(\mathbf{0}, \mathbf{I})$. The variational parameters μ_{ψ} and Σ_{ψ} are learned by minimizing the loss (Dalca et al. 2019):

$$\begin{aligned} \mathcal{L}_{\text{prob.}}(I_f, I_m, \phi_{\mathbf{u}}; \psi) &= -\mathbb{E}_{\mathbf{u} \sim q_{\psi}} \left[\log p(I_f|\mathbf{u}, I_m) \right] + \text{KL} \left[q_{\psi}(\mathbf{u}|I_f, I_m) \parallel p(\mathbf{u}) \right] \\ &= \frac{1}{2\sigma^2} \|I_f - I_m \circ \phi_{\mathbf{u}}\|^2 + \frac{1}{2} \left[\text{tr}(\lambda \mathbf{D} \Sigma_{\psi} - \log \Sigma_{\psi}) + \mu_{\psi}^{\top} \Lambda_{\mathbf{u}} \mu_{\psi} \right], \end{aligned} \quad (25)$$

where $\mu_{\psi}^{\top} \Lambda_{\mathbf{u}} \mu_{\psi}$ can be think of as a diffusion regularization (Eqn. 16) placed over the mean displacement field μ_{ψ} , that is $\mu_{\psi}^{\top} \Lambda_{\mathbf{u}} \mu_{\psi} = \frac{\lambda}{2} \sum_{\mathbf{p}} \sum_{i \in N_{\mathbf{p}}} (\mu(\mathbf{p}) - \mu(i))^2$, where $N_{\mathbf{p}}$ represents the neighboring voxels of the \mathbf{p}^{th} voxel.

As discussed in section 3.2.3, when the auxiliary segmentation information is available (i.e., the label maps of I_f and I_m , denoted as s_f and s_m), Dice loss can be used for training the network to further enhance registration performance. Dice loss, however, does not preserve a Gaussian approximation. Instead, we follow (Dalca et al. 2019) and replace the KL divergence in Eqn. 23 with:

$$\text{KL} \left[q_{\psi}(\mathbf{u}|I_f, I_m) \parallel p(\mathbf{u}|I_f, s_f; I_m, s_m) \right], \quad (26)$$

which yields a loss function of the form:

$$\begin{aligned} \mathcal{L}_{\text{prob. w/ aux.}}(I_f, s_f, I_m, s_m, \phi_{\mathbf{u}}; \psi) &= \frac{1}{2\sigma^2} \|I_f - I_m \circ \phi_{\mathbf{u}}\|^2 + \frac{1}{2\sigma_s^2} \|s_f - s_m \circ \phi_{\mathbf{u}}\|^2 \\ &+ \frac{1}{2} \left[\text{tr}(\lambda \mathbf{D} \Sigma_{\psi} - \log \Sigma_{\psi}) + \mu_{\psi}^{\top} \Lambda_{\mathbf{u}} \mu_{\psi} \right]. \end{aligned} \quad (27)$$

In (Dalca et al. 2019), s_f and s_m represent *anatomical surfaces* originated from label maps. In contrast, we directly used the *label maps* as s_f and s_m in this work. They are image volumes with multiple channels, each channel containing a binary mask defining the segmentation of a certain structure/organ.

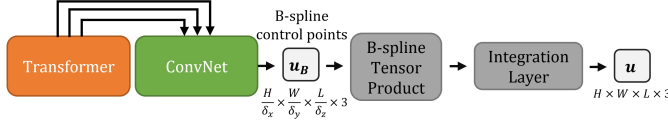


Fig. 7. The architecture of the B-spline diffeomorphic TransMorph.

3.3.2. B-splines diffeomorphic registration

We incorporated a cubic B-spline model (Qiu et al. 2021) to TransMorph (which we denote as TransMorph-bspl.), in which the network produces a lattice of low-dimensional control points instead of producing a dense displacement field at the original resolution, which might be computationally costly. As shown in Fig. 7, we denote the displacements of the B-spline control points generated by the network as \mathbf{u}_B and the spacing between the control points as δ . Then, a weighted combination of cubic B-spline basis functions (i.e., β_d) (Rueckert et al. 1999) is used to generate the dense displacement field (i.e., the B-spline tensor product in Fig. 7):

$$\hat{\mathbf{u}}(\mathbf{p}) = \sum_{\mathbf{c} \in C} \mathbf{u}_B(\mathbf{c}) \prod_{d \in \{x, y, z\}} \beta_d(\mathbf{p}_d - k(\mathbf{c}_d)), \quad (28)$$

where \mathbf{c} is the index of the control points on the lattice C , and k denotes the coordinates of the control points $\mathbf{u}_B(\mathbf{c})$ in image space. Then the final time-stationary displacement \mathbf{u} is obtained using the same *scaling-and-squaring* approach described in section 2.1.2.

3.4. Bayesian Uncertainty Variant

In this section, We extend the proposed TransMorph to a Bayesian neural network (BNN) using the variational inference framework with Monte Carlo dropout (Gal and Ghahramani 2016). We denoted the resulting model as TransMorph–Bayes. In this model, Dropout layers were inserted into the Transformer encoder of the TransMorph architecture but not into the ConvNet decoder, in order to avoid imposing excessive regularity for the network parameters and thus decreasing performance. We briefly review the fundamental ideas in the following paragraph, but we refer readers to (Gal and Ghahramani 2016) for more details. Given a training dataset of moving and fixed images $\mathcal{D} = (\mathbf{I}_m, \mathbf{I}_f)$, where $\mathbf{I}_m = \{I_m^1, I_m^2 \dots I_m^N\}$ represents the moving images, the corresponding target images is denoted by $\mathbf{I}_f = \{I_f^1, I_f^2 \dots I_f^N\}$, and N is the number of image pairs. We aim to find the predictive distribution of the form $p(I_f | I_m, \mathcal{D})$, which can be computed as:

$$p(I_f | I_m, \mathcal{D}) = \int p(I_f | I_m, \mathbf{w}) p(\mathbf{w} | \mathcal{D}) d\mathbf{w}, \quad (29)$$

where $\mathbf{w} = \{\mathbf{W}_1, \mathbf{W}_2 \dots \mathbf{W}_N\}$ denotes the weight matrices in the Transformer encoder. However, this integral over \mathbf{w} is computationally intractable since one would need to sample a large number of networks with various configurations of the parameters to get an accurate estimate of the predictive distribution. Since the distribution $p(\mathbf{w} | \mathcal{D})$ cannot be evaluated analytically, we define an variational distribution $q(\mathbf{w})$ that follows a Bernoulli distribution:

$$q(\mathbf{W}_i) = \mathbf{M}_i \cdot \text{diag}([z_{i,j}]_{j=1}^{K_i}), \quad z_{i,j} \sim \text{Bern}(p), \quad (30)$$

where \mathbf{M}_i is the i^{th} weight, K_i is chosen so that the dimensions of \mathbf{M}_i and $z_{i,j}$ are match, and p is the probability that $z_{i,j} = 0$. It has been shown in (Gal and Ghahramani 2016) that ELBO maximization may be accomplished via training and inferencing with dropout (Srivastava et al. 2014). In the Transformer encoder of TransMorph, we added a dropout layer after each fully connected layer in the MLPs (Eqn. 9) and after each self-attention computation (Eqn. 10). Note that these are the locations where dropout are commonly used for Transformer training. We set the dropout probability p at 0.15 to further avoid the network imposing an excessive degree of regularity on the network weights. The predictive mean can be estimated by using Monte Carlo integration (Gal and Ghahramani 2016):

$$\hat{I}_f = \frac{1}{T} \sum_{t=1}^T I_m \circ \phi_t. \quad (31)$$

This is equivalent to averaging the output of T forward passes through the network during inference, where ϕ_t represents the deformation field produced by t^{th} forward pass. The registration uncertainty can be estimated using the predictive variance as in (Yang et al. 2017b, 2016, 2017a; Sentker et al. 2018; Sedghi et al. 2019):

$$\hat{\Sigma}_f^2 = \frac{1}{T} \sum_{t=1}^T (I_m \circ \phi_t - \hat{I}_f)^2. \quad (32)$$

3.4.1. Uncertainty calibration

Estimating the uncertainty in image registration allows for evaluating the trustworthiness of the registered image, which enables the assessment of operative risks and leads to better-informed clinical decisions (Luo et al. 2019). An ideal uncertainty estimate should be properly correlated to the inaccuracy of the registration results; that is, a high uncertainty value should indicate a large registration error, and vice versa. Otherwise, doctors/surgeons may be misled by the erroneous estimate of registration uncertainty and place unwarranted confidence in the registration results, resulting in severe consequences (Luo et al. 2019; Risholm et al. 2013, 2011). The uncertainty given by Eqn. 32 is expressed as the variability from the mean model prediction. Such an uncertainty estimation does not account for the systematic errors (i.e., bias) between the mean registration prediction and the target image; therefore, a low uncertainty value given by Eqn. 32 does not always guarantee an accurate registration result.

When the predicted uncertainty values closely corresponded with the expected model error, they are considered to be well-calibrated (Laves et al. 2019; Levi et al. 2019). In an ideal scenario, the estimated registration uncertainty should completely reflect the actual registration error. For instance, if the predictive variance of a batch of registered images generated by the network is found to be 0.5, the expectation of the squared error should likewise be 0.5. Accordingly, if the expected model error is quantified by MSE, then the perfect calibration of predictive registration uncertainty may be established by extending the definitions presented in (Guo et al. 2017; Levi et al. 2019; Laves et al. 2020c):

$$\mathbb{E}_{\hat{\Sigma}^2} [\|I_m \circ \phi - I_f\|^2 | \hat{\Sigma}^2 = \Sigma^2] = \Sigma^2 \quad \forall \{\Sigma^2 \in \mathbb{R} | \Sigma^2 \geq 0\}. \quad (33)$$

Model	Conv. skip.	Trans. skip.	Parameters (M)
TransMorph	✓	✓	46.77
TransMorph w/o conv. skip.	✓	-	46.70
TransMorph w/o Trans. skip.	-	✓	41.55
TransMorph w/ lrn. positional embedding	✓	✓	63.63
TransMorph w/ sin. positional embedding	✓	✓	46.77

Table 1. The ablation study of TransMorph models with skip connections and positional embedding. "Conv. skip." denotes the skip-connections from convolutional layers (indicated by green arrows in Fig. 2); "Trans. skip," denotes the skip-connections from the Transformer blocks (indicated by orange arrows in Fig. 2); "lrn. positional embedding" denotes the learnable positional embedding; "sin. positional embedding" denotes the sinusoidal positional embedding.

Model	Embed. Dimension	Swin-T. block numbers	Head numbers	Parameters (M)
TransMorph	96	{2, 2, 4, 2}	{4, 4, 8, 8}	46.77
TransMorph-tiny	6	{2, 2, 4, 2}	{4, 4, 8, 8}	0.24
TransMorph-small	48	{2, 2, 4, 2}	{4, 4, 4, 4}	11.76
TransMorph-large	128	{2, 2, 12, 2}	{4, 4, 8, 16}	108.34
VoxelMorph-huge	-	-	-	63.25

Table 2. The architecture hyper-parameters of the TransMorph models used in the ablation study. "Embed. Dimension" denotes the embedding dimension, C , in the very first stage (described in section 3.2); "Swin-T." denotes Swin Transformer.

In the conventional paradigm of Bayesian neural network, the uncertainty estimate is derived from the predictive variance $\hat{\Sigma}^2$ relative to the predictive mean \hat{I}_f as in Eqn. 32. However, it can be shown that this predictive variance may be miscalibrated as a result of overfitting the training dataset (as shown in Appendix B). Therefore, the uncertainty values estimated based on $\hat{\Sigma}_f^2$ in Eqn. 32 may be biased. This bias often needs to be corrected in many applications, such as image denoising or classification (Laves et al. 2019; Guo et al. 2017; Kuleshov et al. 2018; Phan et al. 2018; Laves et al. 2020c,a), such that the uncertainty values closely reflect the expected error. In image registration, however, the expected error may be computed even during the test time since the target image is always known. Therefore, a perfectly calibrated uncertainty quantification may be achieved without additional effort. Here, we propose to replace the predicted mean \hat{I}_f with the target image I_f in Eqn. 32. Then, the estimated registration uncertainty is the equivalent to the expected error:

$$\Sigma_f^2 = \text{err}(I_m \circ \phi) = \frac{1}{T} \sum_{t=1}^T (I_m \circ \phi_t - I_f)^2. \quad (34)$$

The comparison between the two uncertainty estimate methods (i.e., $\hat{\Sigma}_f^2$ and Σ_f^2) is shown later in this paper.

4. Experiments

4.1. Datasets and Preprocessing

Two datasets including over 1000 image pairs were used to thoroughly validate the proposed method. The details of each dataset are described in the following sections.

4.1.1. Inter-patient Brain MRI Registration

For the inter-patient brain MR image registration task, we used a dataset of 260 T1-weighted brain MRI images acquired from Johns Hopkins University. The dataset was split into 182,

26, and 52 (7:1:2) volumes for training, validation, and test sets. Each image volume was randomly matched to two other volumes in the set to form four registration pairs of I_f and I_m , resulting in 768, 104, and 208 image pairs. FreeSurfer (Fischl 2012) was used to perform standard pre-processing procedures for structural brain MRI, including skull stripping, resampling, and affine transformation. The pre-processed image volumes were then cropped to equal size of 160×192×224. Label maps including 29 anatomical structures were obtained using FreeSurfer for evaluating registration performances.

4.1.2. XCAT-to-CT Registration

Computerized phantoms have been widely used in the medical imaging field for algorithm optimization and imaging system validation (Christoffersen et al. 2013; Chen et al. 2019; Zhang et al. 2017). The four-dimensional extended cardiac-torso (XCAT) phantom (Segars et al. 2010) was developed based on anatomical images from the Visible Human Project data. While the current XCAT phantom¹ can model anatomical variations through organ and phantom scaling, they can not completely replicate the anatomical variations seen in humans. As a result, XCAT-to-CT registration (which can be thought of as atlas-to-image registration) has become a key method for creating anatomically variable phantoms (Chen et al. 2020; Fu et al. 2021; Segars et al. 2013). This research used a CT dataset from (Segars et al. 2013), which includes 50 non-contrast chest-abdomen-pelvis (CAP) CT scans collected from the Duke University imaging database. Selected organs and structures were manually segmented in each patient's CT scan. The structures segmented included the following: the body outline, the bone structures, lungs, heart, liver, spleen, kidneys, stomach, pancreas, large intestine, prostate, bladder, gall bladder, and thyroid. The manual segmentation was done by several medical students, and the results were subsequently corrected by

¹as of October, 2021

an experienced radiologist at Duke University. The CT volumes have voxel sizes ranging from $0.625 \times 0.625 \times 5\text{mm}$ to $0.926 \times 0.926 \times 5\text{mm}$. We used trilinear interpolation to resample all volumes to an identical voxel spacing of $2.5 \times 2.5 \times 5\text{mm}$. The volumes were then cropped and zero-padded to have an equivalent size of $160 \times 160 \times 160$ voxels. The intensity values were first clipped in the range of $[-1000, 700]$ Hounsfield Units and then normalized to the range of $[0, 1]$. The XCAT attenuation map was generated with a resolution of $1.1 \times 1.1 \times 1.1\text{mm}$ using the material compositions and attenuation coefficients of the constituents at 120 keV. It is then resampled, cropped, and padded so that the resulting volume matches the size of the CT volumes. The XCAT attenuation map's intensity values were also normalized to be within a range of $[0, 1]$. The XCAT and CT images are affinely aligned using the proposed affine network. The dataset was split into 35, 5, and 10 (7:1:2) volumes for training, validation, and testing. We conducted five-fold cross-validation on the fifty image volumes, resulting in 50 testing volumes in total.

4.2. Baseline Methods

To illustrate TransMorph's effectiveness, we compared it to various registration methods that have previously demonstrated state-of-the-art registration performances. We begin by comparing TransMorph with four non-deep-learning-based methods, and their hyperparameter settings are described below:

- SyN² (Avants *et al.* 2008): For brain MR registration, we used the mean squared difference (MSQ) as the objective function, along with a Gaussian smoothing of 3 and three scales with 180, 80, 40 iterations, respectively. For XCAT-to-CT registration, we used the cross-correlation (CC) as the objective function, along with a Gaussian smoothing of 5 and three scales with 160, 100, 40 iterations, respectively.
- NiftyReg³ (Modat *et al.* 2010): We employed the sum of squared differences (SSD) as the objective function and bending energy as a regularizer for both tasks. For brain MR registration, we used a regularization weighting of 0.0002 and three scales with 300 iterations each. For XCAT-to-CT registration, we used a regularization weight of 0.0005 and five scales with 500 iterations each.
- deedsBCV⁴ (Heinrich *et al.* 2015): The objective function was self-similarity context (SSC) (Heinrich *et al.* 2013b) by default. For brain MR registration, we used the hyperparameter values suggested in (Hoffmann *et al.* 2020) for neuroimaging, in which the grid spacing, search radius, and quantization step are set to $6 \times 5 \times 4 \times 3 \times 2$, $6 \times 5 \times 4 \times 3 \times 2$, and $5 \times 4 \times 3 \times 2 \times 1$, respectively. For XCAT-to-CT registration, we used the default parameters suggested for abdominal CT registration, where the grid spacing, search radius, and quantization step are $8 \times 7 \times 6 \times 5 \times 4$, $8 \times 7 \times 6 \times 5 \times 4$, and $5 \times 4 \times 3 \times 2 \times 1$, respectively.

²<https://github.com/ANTsX/ANTsPy>

³<https://www.ucl.ac.uk/medical-image-computing>

⁴<https://github.com/mattiaspaul/deedsBCV>

- LDDMM⁵ (Beg *et al.* 2005): MSE was used as the objective function by default. For brain MR registration, we used the smoothing kernel size of 5, the smoothing kernel power of 2, the matching term coefficient of 4, the regularization term coefficient of 10, and the iteration number of 500. For XCAT-to-CT registration, we used the same kernel size, kernel power, the matching term coefficient, and the number of iteration. However, the regularization term coefficient was empirically set to 3.

Next, we compared the proposed method with several existing deep-learning-based methods. For a fair comparison, unless otherwise indicated, the loss function (Eqn. 13) that consists of MSE (Eqn. 14) and diffusion regularization (Eqn. 16) was used to register brain MR, while the loss function (Eqn. 18) that consists of LNCC (Eqn. 15), bending energy (Eqn. 17), and Dice (Eqn. 19) was used for XCAT-to-CT registration. Auxiliary data (organ segmentation) was used for XCAT-to-CT registration. Recall that the hyperparameters λ and γ define, respectively, the weight for deformation field regularization and Dice loss. The detailed parameter settings of each method are as follows:

- VoxelMorph⁶ (Balakrishnan *et al.* 2018, 2019): We employed two variants of VoxelMorph, the second of which twice the number of convolution filters in the first variant; they are designated as VoxelMorph-1 and -2, respectively. For brain MR registration, the regularization hyperparameter λ was set to 0.02, which was reported as an optimal value in the VoxelMorph paper. For XCAT-to-CT registration, we set $\lambda = \gamma = 1$.
- VoxelMorph-diff⁷ (Dalca *et al.* 2019): For brain MR registration task, the loss function \mathcal{L}_{prob} (Eqn. 25) was used with σ set to 0.01 and λ set to 20. For XCAT-to-CT registration, we used the loss function $\mathcal{L}_{prob,w/aux}$ (Eqn. 27) with $\sigma = \sigma_s = 0.01$ and $\lambda = 20$.
- CycleMorph⁸ (Kim *et al.* 2021): In CycleMorph, the hyperparameters α , β , and λ , correspond to the weights for cycle loss, identity loss, and deformation field regularization. We chose the optimal α and β values reported in Kim *et al.* 2021, and λ was set empirically because the default values were found to be sub-optimal for applying CycleMorph to our dataset. For brain MR registration, we set $\alpha = 0.1$, $\beta = 0.5$, and $\lambda = 0.02$. Whereas for XCAT-to-CT registration, we modified the CycleMorph by adding a Dice loss with a weighting of 1 to incorporate organ segmentation during training, and we set $\alpha = 0.1$ and $\beta = 1$. We observed that the λ value of 1 suggested in Kim *et al.* 2021 yielded over-smoothed deformation field in our application. Therefore, the value of λ was decreased to 0.1.
- MIDIR⁹ (Qiu *et al.* 2021): The same loss function and λ value as VoxelMorph were used. In addition, the control

⁵<https://github.com/brianlee324/torch-lddmm>

⁶<http://voxelmorph.csail.mit.edu>

⁷<http://voxelmorph.csail.mit.edu>

⁸https://github.com/boahK/MEDIA_CycleMorph

⁹<https://github.com/qiuhuaqi/midir>

point spacing δ for B-spline transformation was set to 2 for both tasks, which was shown to be an optimal value in Qiu et al. 2021.

To show that the proposed Swin-Transformer-based network architecture outperforms other Transformer models, we compared its performance to other existing Transformer-based networks that achieved state-of-the-art performance in other applications (e.g., image segmentation, object detection, etc.). We customized these models to make them suitable for image registration. They were modified to produce 3-dimensional deformation fields that warp the given moving image. Note that the only change between the methods below and VoxelMorph is the network architecture, with the spatial transformation function, loss function, and network training procedures remaining the same. The first three models use the hybrid Transformer-ConvNet architecture (i.e., ViT-V-Net, PVT, and CoTr), while the last model uses a pure Transformer-based architecture (i.e., nnFormer). Their network hyperparameter settings are as follows:

- ViT-V-Net¹⁰ (Chen et al. 2021a): This registration network was developed based on ViT (Dosovitskiy et al. 2020). For brain MR registration, we applied the default hyperparameter settings suggested in (Chen et al. 2021a).
- PVT¹¹ (Wang et al. 2021c): The default settings were applied, except that the embedding dimensions were to be {20, 40, 200, 320}, the number of heads was set to {2, 4, 8, 16}, and the depth was increased to {3, 10, 60, 3}.
- CoTr¹² (Xie et al. 2021): We used the default network settings for both brain MR and XCAT-to-CT registration tasks.
- nnFormer¹³ (Zhou et al. 2021): Because nnFormer was also developed on the basis of Swin Transformer, we applied the same Transformer parameter values as in TransMorph to make a fair comparison.

4.3. Implementation Details

The proposed TransMorph was implemented using PyTorch (Paszke et al. 2019) on a PC with an NVIDIA TITAN RTX GPU and an NVIDIA RTX3090 GPU. All models were trained for 500 epochs using the Adam optimization algorithm, with a learning rate of 1×10^{-4} and a batch size of 1. The brain MR dataset was augmented with flipping in random directions during training, while no data augmentation was applied to the CT dataset. Restricted by the sizes of the image volumes, the window sizes (i.e., $\{M_x, M_y, M_z\}$) used in Swin Transformer were set to {5, 6, 7} for MR brain registration and {5, 5, 5} for XCAT-to-CT registration, respectively. The Transformer hyperparameter settings for TransMorph is listed in the first row of Table. 2. Note that the variants of TransMorph (i.e., TransMorph-Bayes, TransMorph-bspl, and TransMorph-diff) share the same Transformer settings as

TransMorph. The hyperparameter settings for each proposed variant are described as follows:

- TransMorph: The identical loss function parameters as VoxelMorph were used for both MR registration and XCAT-to-CT registration tasks.
- TransMorph-Bayes: The identical loss function parameters as VoxelMorph were applied here for both tasks. The dropout probability (i.e., p in Eqn. 30) was set to 0.15.
- TransMorph-bspl: Again, the loss function settings for both tasks were the same as those used in VoxelMorph. The control point spacing, δ , for B-spline transformation was also set to 2, the same value used in MIDIR.
- TransMorph-diff: We applied the same loss function parameters as those used in VoxelMorph-diff.

The affine model presented in this work comprises of a compact Swin Transformer. The Transformer parameter settings were identical to TransMorph except that the embedding dimension was set to be 12, the numbers of Swin Transfomer block were set to be {1, 1, 2, 2}, and the head numbers were set to be {1, 1, 2, 2}. The resulting affine model has a total number of parameters. Because the MRI datasets were affinely aligned as part of the preprocessing, the affine model was only used in the XCAT-to-CT registration.

4.4. Additional Studies

In this section, we design experiments to verify the effect of Transformer modules in TransMorph architecture. Specifically, we performed two additional studies on model complexity and network components. They are described in the following subsections.

4.4.1. Ablation study on network components

We begin by examining the effects of several network components on registration performance. Table 1 listed three variants of TransMorph by either keeping or removing the network's long skip connections or the positional embeddings in the Transformer encoder. In "TransMorph w/o conv. skip.", the long skip connections from the two convolutional layers were removed (including two convolutional layers), which are the green arrows in Fig. 2. In "TransMorph w/o trans. skip.", the long skip connections coming from the Swin Transformer blocks were removed, which are the orange arrows in Fig. 2. We hypothesized in section 3.2 that the positional embedding (i.e., E_{pos} in Eqn. 8) is not a necessary element of TransMorph, because the positional information of tokens can be learned implicitly in the network via the consecutive up-sampling in the decoder and backpropagating the loss between output and target. Here, we conducted experiments to study the effectiveness of positional embeddings. In the second to last variant, "TransMorph w/ lrn. positional embedding", we used a learnable positional embedding in the Transformer encoder, the same one used in the Swin Transformer (Liu et al. 2021a). In the last variant, "TransMorph w/ sin. positional embedding", we substituted the learnable positional embedding with a sinusoidal positional embedding, the same embedding used in the original Transformer (Vaswani et al. 2017), which hardcodes the positional information in the tokens.

¹⁰<https://bit.ly/3bWDynR>

¹¹<https://github.com/whai362/PVT>

¹²<https://github.com/YtongXie/CoTr>

¹³<https://github.com/282857341/nnFormer>

Model	DSC	% of $ J_\phi \leq 0$
Affine	0.572 \pm 0.166	-
SyN	0.722 \pm 0.127	<0.0001
NiftyReg	0.716 \pm 0.131	0.061 \pm 0.093
LDDMM	0.710 \pm 0.131	<0.0001
deedsBCV	0.719 \pm 0.130	0.253 \pm 0.110
VoxelMorph-1	0.711 \pm 0.134	0.426 \pm 0.231
VoxelMorph-2	0.716 \pm 0.133	0.389 \pm 0.222
VoxelMorph-diff	0.706 \pm 0.136	<0.0001
CycleMorph	0.717 \pm 0.134	0.231 \pm 0.168
MIDIR	0.704 \pm 0.131	<0.0001
ViT-V-Net	0.729 \pm 0.128	0.402 \pm 0.249
PVT	0.722 \pm 0.130	0.427 \pm 0.254
CoTr	0.718 \pm 0.131	0.415 \pm 0.258
nnFormer	0.722 \pm 0.128	0.399 \pm 0.234
TransMorph-Bayes	0.736 \pm 0.125	0.389 \pm 0.241
TransMorph-diff	0.723 \pm 0.128	<0.0001
TransMorph-bspl	0.733 \pm 0.124	<0.0001
TransMorph	0.737\pm0.125	0.396 \pm 0.240

Table 3. Quantitative evaluation results on inter-patient brain MRI registration. Dice score and percentage of voxels with a non-positive Jacobian determinant (i.e., folded voxels) are evaluated for different methods. The bolded numbers denote the highest scores, while the *italicized* ones indicate the second highest.

4.4.2. Model complexity study

The impact of model complexity on registration performance was also investigated in this paper. Table 2 listed the parameter settings and the number of trainable parameters of four variants of the proposed TransMorph model. In the base model, TransMorph, the embedding dimension C was set to 96, and the number of Swin Transformer blocks in the four stages of the encoder was set to 2, 2, 4, and 2, respectively. Additionally, we introduced TransMorph-tiny, TransMorph-small, and TransMorph-large, which are about 1/200 \times , 1/4 \times , and 2 \times the model size of TransMorph. Finally, we compared our model to a customized VoxelMorph (denoted as VoxelMorph-huge), which has a comparable parameter size to that of TransMorph w/ lrn. positional embedding. Specifically, we maintained the same number of layers in VoxelMorph-huge as in VoxelMorph, but increased the number of convolution kernels in each layer. As a result, VoxelMorph-huge has 63.25 million trainable parameters.

5. Results

5.1. Inter-patient Brain MRI Registration

The left panel of Fig. 8 shows the qualitative registration results on an example brain MRI slice. The scores in blue, orange, green, and pink correspond to ventricles, third ventricle, thalamus, and hippocampi, respectively. Additional qualitative comparisons across all methods are shown in Fig. C.19 in Appendix. Among the proposed models, diffeomorphic variants (i.e., TransMorph-diff and TransMorph-bspl) generated smoother displacement fields, with TransMorph-bspl producing the smoothest deformations inside the brain area. On the other hand, TransMorph and TransMorph-Bayes showed

Model	DSC	% of $ J_\phi \leq 0$	SSIM
w/o registration	0.220 \pm 0.242	-	0.576 \pm 0.071
Affine Transformer	0.330 \pm 0.291	-	0.751 \pm 0.018
SyN	0.494 \pm 0.341	<0.0001	0.894 \pm 0.021
NiftyReg	0.482 \pm 0.341	<0.0001	0.886 \pm 0.027
LDDMM	0.411 \pm 0.341	0.006 \pm 0.007	0.874 \pm 0.031
deedsBCV	0.568 \pm 0.306	0.001 \pm 0.001	0.863 \pm 0.029
VoxelMorph-1	0.533 \pm 0.312	0.023 \pm 0.013	0.899 \pm 0.027
VoxelMorph-2	0.549 \pm 0.310	0.017 \pm 0.009	0.910 \pm 0.027
VoxelMorph-diff	0.528 \pm 0.328	<0.0001	0.911 \pm 0.020
CycleMorph	0.531 \pm 0.321	0.033 \pm 0.012	0.909 \pm 0.024
MIDIR	0.547 \pm 0.306	<0.0001	0.896 \pm 0.022
ViT-V-Net	0.579 \pm 0.315	0.014 \pm 0.006	0.915 \pm 0.020
PVT	0.527 \pm 0.317	0.029 \pm 0.012	0.900 \pm 0.027
CoTr	0.559 \pm 0.312	0.015 \pm 0.011	0.905 \pm 0.029
nnFormer	0.547 \pm 0.311	0.014 \pm 0.006	0.902 \pm 0.024
TransMorph-Bayes	0.595 \pm 0.313	0.015 \pm 0.009	0.919\pm0.024
TransMorph-diff	0.541 \pm 0.325	<0.0001	0.910 \pm 0.025
TransMorph-bspl	0.575 \pm 0.308	<0.0001	0.908 \pm 0.025
TransMorph	0.598\pm0.313	0.017 \pm 0.008	0.918 \pm 0.023

Table 4. Quantitative evaluation results on XCAT-to-CT registration. Dice score of 16 organs and percentage of voxels with a non-positive Jacobian determinant (i.e., folded voxels) are evaluated for different methods. The bolded numbers denote the highest scores, while the *italicized* ones indicate the second highest.

better visual results with higher Dice scores for the highlighted structures.

The quantitative evaluations are shown in Table 3. Overall, the results presented in the table show that the proposed method, TransMorph, achieved the highest Dice score of 0.737. Although the diffeomorphic variants produced slightly lower Dice scores than TransMorph, they still outperformed the existing registration methods and generated almost no foldings (i.e., $\sim 0\%$ of $|J_\phi| \leq 0$) in deformation fields. By comparison, TransMorph improved performance by >0.1 when compared to VoxelMorph and by >0.3 when compared to CycleMorph. We found that the Transformer-based models (i.e., TransMorph, ViT-V-Net, PVT, CoTr, and nnFormer) generally produced better Dice scores than the ConvNet-based models. Note that even though ViT-V-Net has almost twice the number of the trainable parameters (as shown in Fig. 9), TransMorph still outperformed all the Transformer-based models (including ViT-V-Net) by at least 0.08 in Dice, demonstrating Swin-Transformer’s superiority over other Transformer architectures. When we conducted hypothesis testing on the results using the paired *t*-test, the *p*-values for TransMorph over all other methods (i.e., non-TransMorph methods) were $p \ll 0.05$, with an exception of TransMorph over ViT-V-Net, which was $p = 0.052$.

Figs. C.20 and C.21 show additional Dice results on a variety of anatomical structures, with Fig. C.20 comparing TransMorph to current registration techniques (both optimization- and learning-based methods), and Fig. C.21 comparing the Dice scores between the Transformer-based models.

5.2. XCAT-to-CT Registration

The right panel of Fig. 8 shows the qualitative results on a representative CT slice. The blue, orange, green, and pink lines denote the liver, heart, left lung, and right lung, respectively,

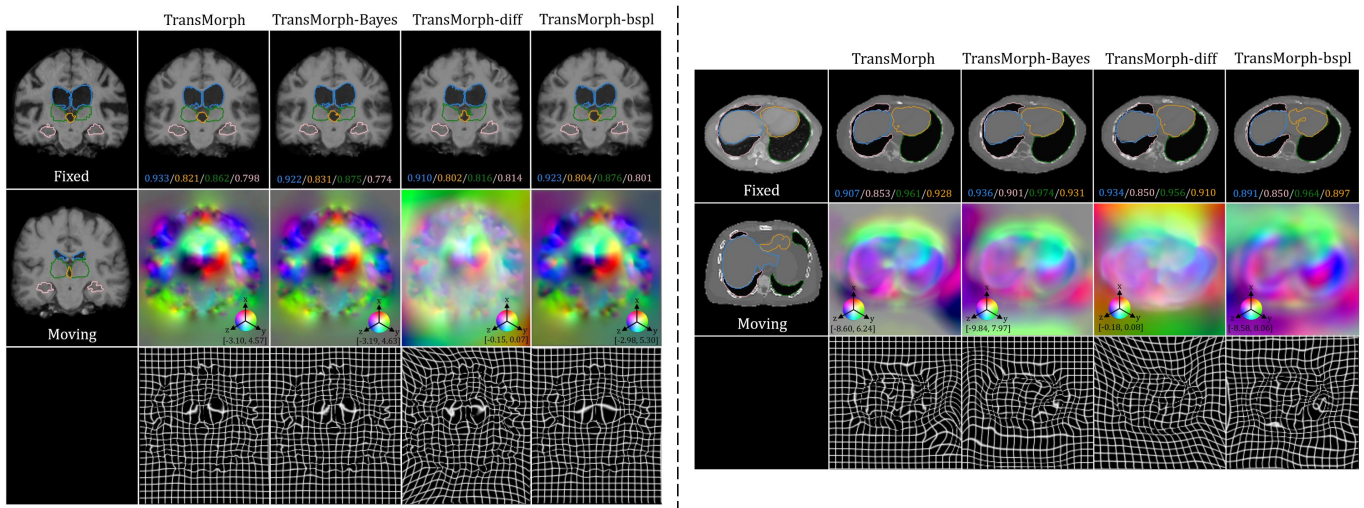


Fig. 8. Qualitative results of TransMorph (2nd column) and its Bayesian- (3rd column), probabilistic- (4th column), and B-spline (5th column) variants. Left panel: Results of inter-patient brain MRI registration. The blue, orange, green, and pink contours define, respectively, the ventricles, third ventricle, thalamus, and hippocampi. Right panel: Results of XCAT-to-CT registration. The blue, orange, green, and pink contours define, respectively, the liver, heart, left lung, and right lung. The second row in both panels exhibits the displacement fields \mathbf{u} , where spatial dimension x , y , and z is mapped to each of the RGB color channels, respectively. The $[p, q]$ in color bars denotes the magnitude range of the fields.

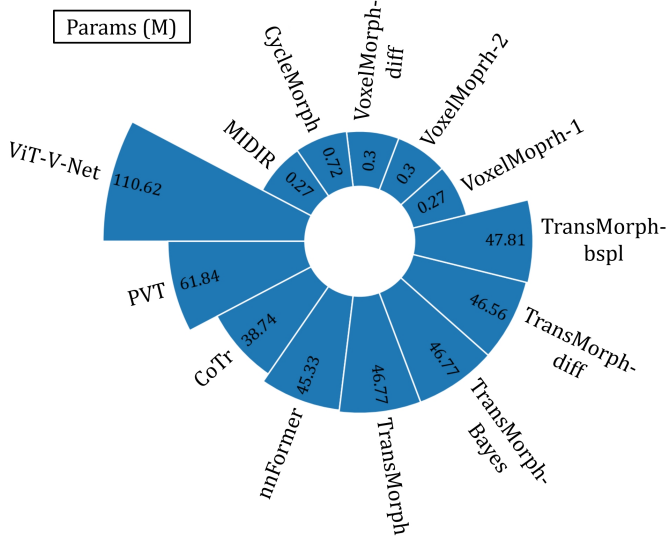


Fig. 9. The number of parameters in each deep-learning-based model. The values are expressed in the form of million parameters.

while the bottom values show the corresponding Dice scores. Similar to the findings in the previous section, TransMorph and TransMorph-Bayes gave more precise registration results, although diffeomorphic variations produced smoother deformations. Additional qualitative comparisons are shown in the Fig. D.22 in the Appendix. It is possible to see certain artifacts in the displacement field created by nnFormer (as shown in Fig. D.22); these are most likely caused by the patch operations of the Transformers used in its architecture. nnFormer is a near-convolution-free model (convolutional layers were employed only to form displacement fields). In contrast to brain MRI registration, displacement in XCAT-to-CT registration may exceed the patch size. As a consequence, the lack of convolutional layers to refine the displacement field may have resulted in those

artifacts. Four example coronal slices of the deformed XCAT phantoms generated by various registration methods are shown in Fig. D.23 in Appendix.

The quantitative evaluation results are presented in Table 4. They include Dice scores for all organs and scans, the percentage of non-positive Jacobian determinants, and the structural similarity index (SSIM) (Wang et al. 2004) between the deformed XCAT phantom and the target CT scan. The window size used in SSIM was set to 7. Without registration or affine transformation, a poor Dice score of 0.22 and an SSIM of 0.576 demonstrate the vast dissimilarity between the original XCAT phantom and patient CT scans. The Dice score and SSIM increased to 0.33 and 0.751, respectively, after aligning the XCAT and patient CT using the proposed affine Transformer. Among the traditional registration methods, deedsBCV, which was initially designed for abdominal CT registration-based segmentation (Heinrich et al. 2015), achieved the highest Dice score of 0.568, which is even higher than most of the learning-based approaches. Among the learning-based approaches, Transformer-based models outperformed ConvNet-based models on average, which is consistent with the previous section's finding in brain MR registration. The p -value from the paired t-test between TransMorph and other learning-based methods were < 0.05 with an exception that p -value=0.158 for ViT-V-Net. The proposed TransMorph models yielded the highest Dice and SSIM scores of all methods on average, with the best Dice of 0.598 given by TransMorph and the best SSIM of 0.919 given by TransMorph-Bayes. The diffeomorphic variants produced lower Dice and SSIM scores as a consequence of not having any folded voxels in the deformation.

Figs. D.24 and D.25 show additional boxplots of Dice scores on the various abdominal organs, with Fig. D.24 comparing TransMorph to current registration techniques (both optimization- and learning-based methods), and Fig. D.25 comparing the Dice scores between the Transformer-based models.

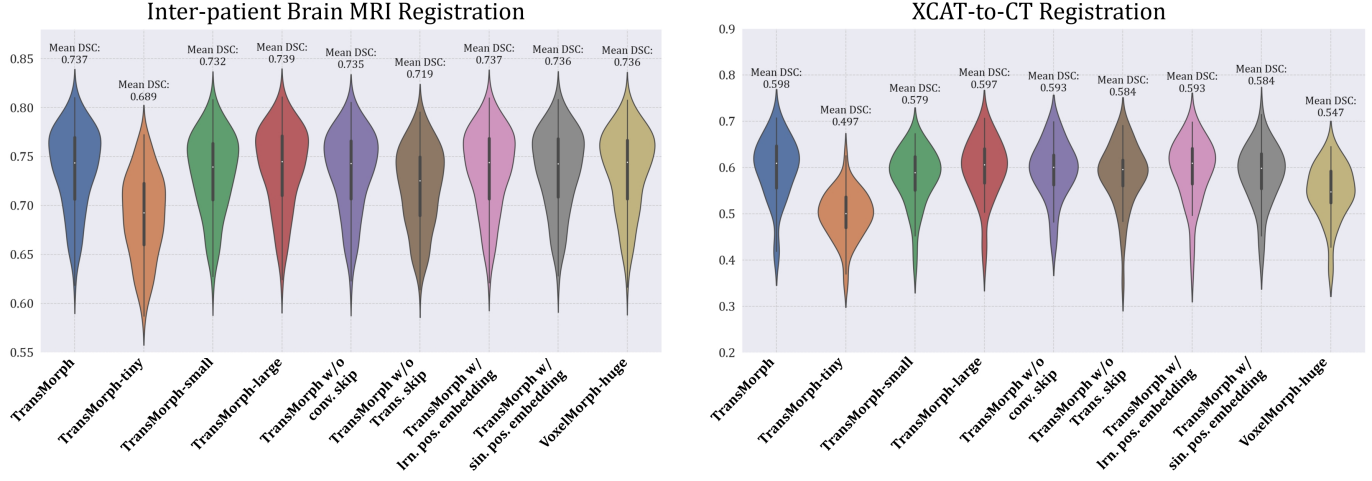


Fig. 10. Quantitative evaluation results of the additional studies on inter-patient brain MRI registration.

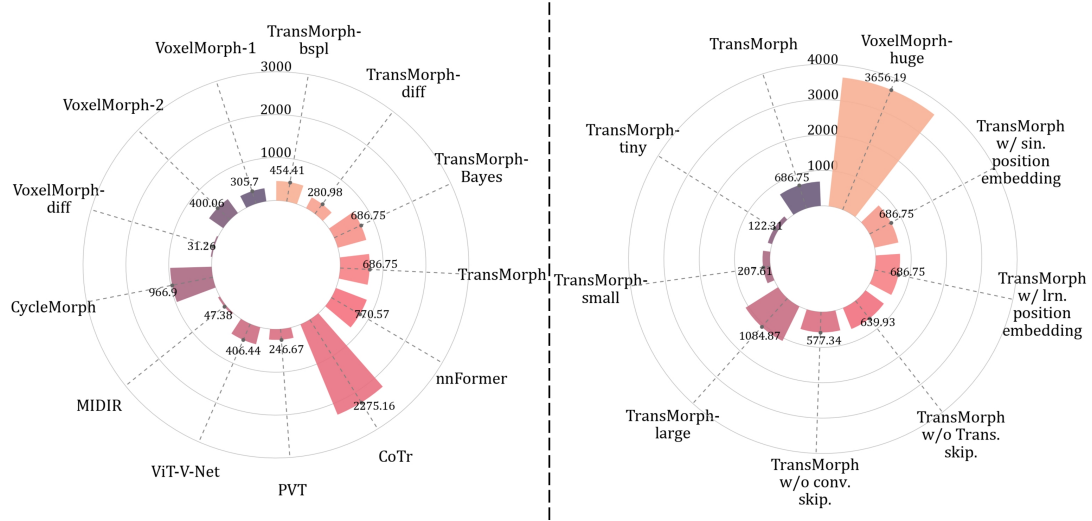


Fig. 11. Model computational complexity comparisons represented in Giga multiply-accumulate operations (GMACs). Greater values imply a greater degree of computational complexity. These values were obtained using an input image of size $160 \times 192 \times 224$.

5.3. Ablation Studies

The left figure in Fig. 10 shows the Dice scores from the ablation study on inter-patient brain MR registration. When evaluating the effectiveness of skip connections, we discovered that the skip connections from both the convolution and Transformer layers might assist with registration performance. TransMorph scored a mean Dice of 0.735 after the skip connections from the convolutional layers were removed. However, the score decreased to 0.719 when the skip connections from the Transformer blocks were removed. In comparison, the efficacy of the skip connections from convolutional layers is less substantial, with a mean DSC improvement of 0.002. Note that TransMorph without using positional embedding achieved the same mean DSC and a very comparable violin plot as TransMorph, suggesting that positional embedding may be an unnecessary component.

The figure on the right in Fig. 10 shows scores from the study on XCAT-to-CT registration. Without the skip connections from the convolution and Transformer layers, the Dice

scores drop by 0.005 and 0.014, respectively, when compared to TransMorph, further supporting that skip connections can improve performance. For XCAT-to-CT registration, TransMorph performed slightly worse with positional embeddings than it did without them, with Dice scores decreasing by 0.005 and 0.004 for learnable and sinusoidal positional embeddings, respectively. More data suggest that positional embedding may be unnecessary for TransMorph. The effect of each component is addressed in depth in the Discussion section (section 6.1).

5.4. Computational Complexity

The circular barplot in the left panel of Fig. 11 shows the computational complexity comparisons between the deep-learning-based registration models. The plot was created using an input image with a resolution of $160 \times 192 \times 224$, the same size as the brain MRI images. The numbers are expressed in Giga multiply-accumulate operations (GMACs), with a higher value indicating a more computationally expensive model that

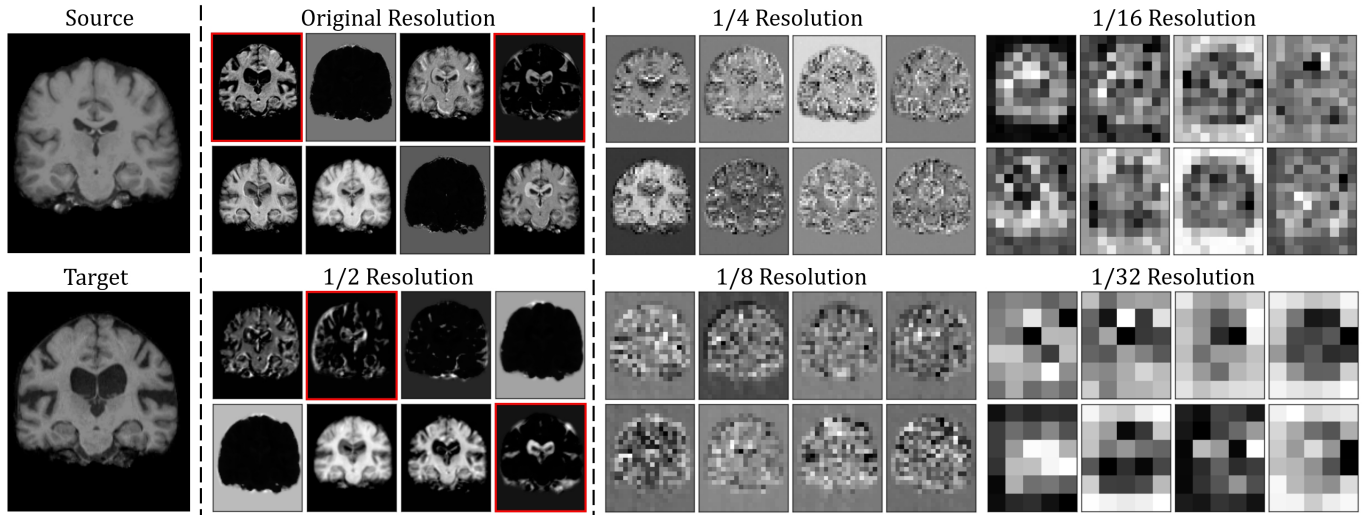


Fig. 12. Examples of feature maps in TransMorph’s skip connections. Eight feature maps are randomly selected from the feature maps associated with each skip connection. Left panel: Example 2D slices of source and target images (i.e., I_m and I_f), which are used as inputs to TransMorph. Middle panel: Feature maps in the skip connections of the two convolutional layers (denoted by the green arrows in Fig. 2). Right panel: Feature maps in the skip connections of the Swin Transformer blocks (denoted by the orange arrows in Fig. 2).

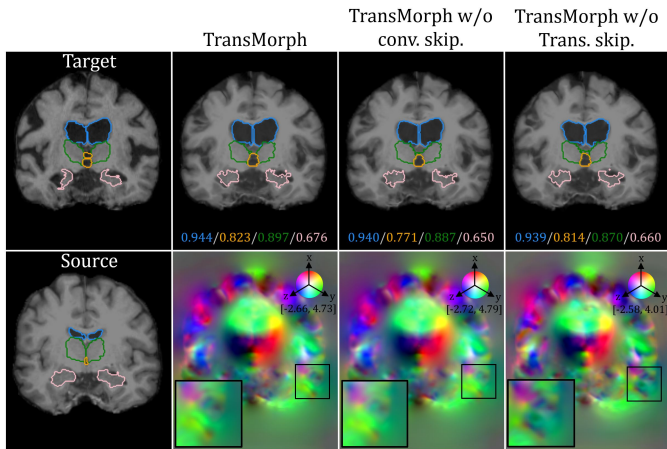


Fig. 13. Qualitative impact of skip connections on the deformation. The spatial dimension x , y , and z in the displacement field is mapped to each of the RGB color channels, respectively. The $[p, q]$ in color bars denotes the magnitude range of the fields.

may also be more memory intensive. The proposed model, TransMorph, and its Bayesian variant, TransMorph–Bayes, have a moderate computational complexity with 687 GMACs which is much less than CoTr and CycleMorph. In practice, the GPU memory occupied during training was about 15 GiB with a batch size of 1 and an input image size of $160 \times 192 \times 224$. The diffeomorphic variants, TransMorph–diff and TransMorph–bspl, have 281 and 454 GMACs, which are comparable to that of the conventional ConvNet-based registration models, VoxelMorph-1 and -2. In practice, they occupied approximately 11 GiB of GPU memory during training, which is a size that can be readily accommodated by the majority of modern GPUs.

Fig. 10 shows the quantitative results of various TransMorph models and the customize ConvNet-based model VoxelMorph-huge on both inter-patient brain MRI and XCAT-to-CT registration.

When parameter size is the only variable in TransMorph models, there is a strong correlation between model complexity (as shown in the right panel of Fig. 11) and registration performance. TransMorph-tiny produced the lowest mean DSC of 0.689 and 0.497 for brain MRI and XCAT-to-CT registration, respectively. The Dice scores steadily improve as the complexity of the model increases. Note that for brain MRI registration (left figure in Fig. 10), the improvement in mean DSC from TransMorph to TransMorph-large is just 0.002 but the latter is almost twice as computationally costly (as shown in the right panel of Fig. 11). Furthermore, TransMorph-large performed very comparable to TransMorph with a difference of 0.001 in Dice for XCAT-to-CT registration. The customized ConvNet-based model, VoxelMorph-huge, achieved a mean DSC close to that of TransMorph for brain MR registration but a suboptimal Dice score of 0.547 for XCAT-to-CT registration. A significant disadvantage of VoxelMorph-huge is its computational complexity, with 3656 GMACs (as seen in the right panel of Fig. 11), it is nearly five times as computationally expensive as TransMorph, making it memory-intensive (~ 22 GiB for a patch size of 1 during training) and slow to train in practice.

6. Discussion

6.1. Network Components in TransMorph

6.1.1. Skip Connections

As previously shown in section 5.3, skip connections may aid in enhancing registration accuracy. In this section, we give further insight into the skip connections’ functionality.

Fig. 12 shows some example feature maps in each skip connection (a full feature map visualization is shown in Fig. G.28 in Appendix). Specifically, the left panel shows sample slices of the input volumes; the center panel illustrates selected feature maps in the skip connections of the convolutional layers, and

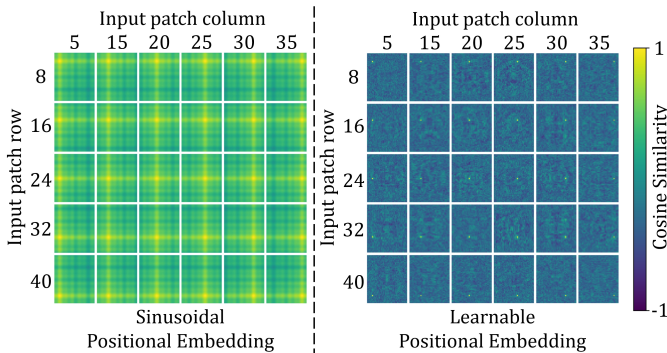


Fig. 14. Example slice of the positional embeddings used in TransMorph. Left panel: Sinusoidal positional embedding. Right panel: Learnable positional embedding. Tiles in both panels show the cosine similarities between the position embedding of the token with the indicated row and column and the position embeddings of all other tokens.

the right panel illustrates selected feature maps in the skip connections of the Swin Transformer blocks. As seen from these feature maps that the Swin Transformer blocks provided more abstract information (right panel in Fig. 12), in comparison to the convolutional layers (middle panel in Fig. 12). Since a Transformer divides an input image volume into patches to create tokens for self-attention operations (as described in section 3.2), it can only deliver information up to a certain resolution, which is often a factor of the patch size lower than the original resolution (i.e., $\frac{H}{P} \times \frac{W}{P} \times \frac{L}{P}$, and $P = 4$ in our case). On the other hand, the convolutional layers resulted in higher resolution feature maps with more detailed and human-readable information (e.g., edge and boundary information). Certain feature maps even revealed distinctions between the moving and fixed images (highlighted by the red boxes). Fig. 13 shows the qualitative comparisons between the proposed model with and without a specific type of skip connection. As seen by the magnified areas, TransMorph with both skip connection types provided a more detailed and accurate displacement field. Therefore, adding skip connections with convolutional layers is still recommended, although the actual DSC improvement were subtle (0.002 for inter-patient brain MRI and 0.003 for XCAT-to-CT registration).

6.1.2. Positional Embedding

Transformers in computer vision were initially designed for image classification tasks (Dosovitskiy *et al.* 2020; Liu *et al.* 2021a; Dong *et al.* 2021; Wang *et al.* 2021c). Such a Transformer produces a condensed probability vector that is not in the image domain but instead a description of the likelihood of being a certain class. The loss calculated based on this vector does not backpropagate any spatial information into the network. Thus, it is critical to encode positional information on the patched tokens; otherwise, as the network gets deeper, Transformer would lose track of the tokens' locations relative to the input image, resulting in unstable training and inferior predictions. However, for pixel-level tasks like image registration, the condensed features generated by Transformers are often subsequently expanded using a decoder whose output is an image with the same resolution as the input and target images. Any

spatial mismatching between the output and target contributes to the loss, which is then backpropagated throughout the network. As a result, the Transformer implicitly learns the positional information of tokens, thus obviating the need for positional embedding. In this work, we compared the registration performance of TransMorph and TransMorph with positional embedding on brain MRI and XCAT-to-CT registration. The results shown in section 5.3 indicated that positional embedding does not improve registration performance; rather, it introduces more parameters into the network. In this section, we discuss the positional embeddings in further detail.

Two positional embeddings were studied in this paper: sinusoidal (Vaswani *et al.* 2017) and learnable (Liu *et al.* 2021a) embeddings, which are also the two major types of positional embedding. In sinusoidal positional embedding, the position of each patched token is represented by a value drawn from a predetermined sinusoidal signal according to the token's position relative to the input image. Whereas with learnable positional embedding, the network learns the representation of the token's location from the training dataset rather than giving a hardcoded value. To validate that the network learned the positional information, Dosovitskiy *et al.* 2020 computed the cosine similarities between a learned embedding of a token and that of all other tokens. The obtained similarity values were then used to form an image. If positional information is learned, the image should reflect increased similarities at the token's and nearby tokens' positions.

Here, we computed the images of cosine similarities for both sinusoidal and learnable positional embeddings used in this work. The left and right panels in Fig. 14 show the images of cosine similarities. These images are generated based on an input image size of $160 \times 192 \times 224$ and a patch size of $4 \times 4 \times 4$ (resulting in $40 \times 48 \times 56$ patches). Each image has a size of 40×48 representing an image of cosine similarities in the plane of $z = 28$ (i.e., the middle slice). There should have been a total of 40×48 images in each panel. However, for better visualization, just a few images are shown here. The images were chosen with step sizes of 5 and 8 in x and y direction, respectively, resulting in 6×5 images in each panel. As seen from the left panel, the images of sinusoidal embeddings exhibit a structured pattern, showing a high degree of correlation between tokens' relative locations and image intensity values. Note that the brightest pixel in each image represents the cosine similarity between a token's positional embedding and itself, which reflects the token's actual location relative to all other tokens. The similarity then gradually decreases as it gets farther away from the token. On the other hand, images generated with learnable embeddings (right panel of Fig. 14) lack such structured patterns, implying that the network did not learn the positional information associated with the tokens in the learnable embeddings. However, as seen from the Dice scores in Fig. 10, regardless of which positional embedding is employed, the mean Dice scores and violin plots are quite comparable to those produced without positional embedding. There is thus evidence that the network learns the positional information of the tokens implicitly, and hence positional embedding is redundant and does not improve registration performance.

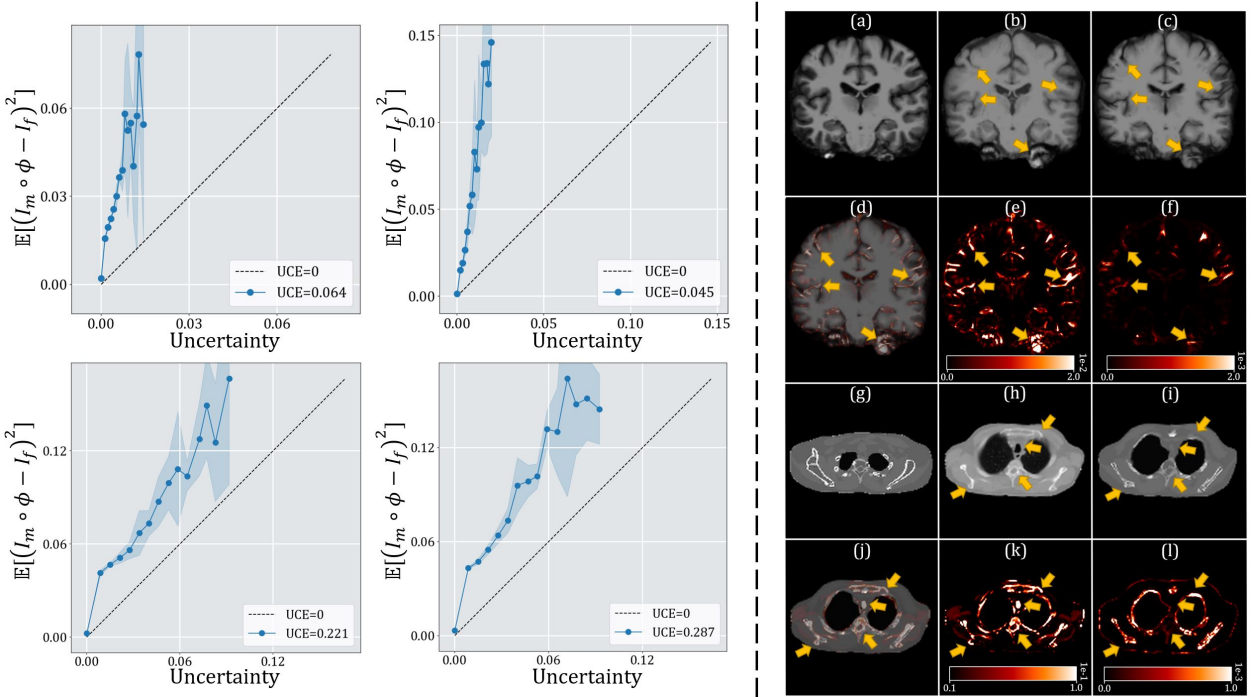


Fig. 15. Comparisons of the uncertainty estimates derived from the predictive variance and the predicted model error. Left panel: Calibration plots and uncertainty calibration error (UCE) for TransMorph-Bayes on two inter-patient brain MR test sets (top) and two XCAT-to-CT test sets (bottom). The blue lines represent the results obtained using the uncertainty estimate $\hat{\Sigma}_f^2$. The dashed lines represent the perfect calibration, where are the results achieved when the uncertainty estimate is Σ_f^2 or $err(I_m \circ \phi)$ (i.e., the expected model error). The values are obtained from 10 repeated runs, and the shaded regions represent the standard deviation. Right panel: Visualization of the registration uncertainty on a brain MRI (i.e., a-f) and a CT (i.e., g-l). (a) & (g): Moving image. (b) & (h): Fixed image. (c) & (i): Deformed moving image. (d) & (j): Per-pixel uncertainty, represented by $\hat{\Sigma}_f^2$, overlays the deformed image. (e) & (k): Per-pixel uncertainty given by $\hat{\Sigma}_f^2$ (i.e., the proposed method). (f) & (l): Per-pixel uncertainty given by $\hat{\Sigma}_f^2$. The yellow arrows highlight sites where $\hat{\Sigma}_f^2$ identifies registration failures but $\hat{\Sigma}_f^2$ does not.

6.2. Uncertainty Quantification of TransMorph-Bayes

As previously mentioned in section 3.4, registration uncertainty estimates produced by the existing method (e.g., (Yang et al. 2017b,a; Sentker et al. 2018; Sedghi et al. 2019)) were actually miscalibrated, meaning that the uncertainty values did not properly correlate to predicted model errors since variance was computed using the predictive mean instead of target image I_f . We proposed to directly use the expected model error to express model uncertainty since the target image is available at all times in image registration. Thus, the resulting uncertainty estimate is perfectly calibrated. In this section, we examine how the proposed and existing methods differ in their estimates of uncertainty.

To quantify the calibration error, we used the Uncertainty Calibration Error (UCE) introduced in (Laves et al. 2020a), which is calculated on the basis of the binned difference between the expected model error (i.e., $E[(I_m \circ \phi - I_f)^2]$) and the uncertainty estimation (e.g., $\hat{\Sigma}_f^2$ in Eqn. 32 or Σ_f^2 in Eqn. 34). We refer the interested reader to the corresponding references for further details about UCE. The plots in the left panel of Fig. 15 exhibit the calibration plots and UCE obtained on four representative test sets. All results are based on a sample size of 25 (i.e., $T = 25$ in Eqn. 31, 32, and 34) from 10 repeated runs. The blue lines show the results produced with the $\hat{\Sigma}_f^2$ and the shaded regions represent the standard deviation from the 10 runs, while

the dashed black lines indicate the perfect calibration achieved with the proposed method. Notice that the uncertainty values obtained using $\hat{\Sigma}_f^2$ do not match well to the expected model error; in fact, they are consistently being underestimated (for reasons described in section 3.4.1). In comparison, the proposed method enables perfect calibration with UCE = 0 since its uncertainty estimate equals the expected model error. In the right panel of Fig. 15, we show the visual comparisons of the uncertainty derived from Σ_f^2 and $\hat{\Sigma}_f^2$. When we compare either (e) to (f) or (k) to (l), we see that the former (i.e., (e) and (k)) captured more registration failures than the latter (as highlighted by the yellow arrows), indicating a stronger correlation between deformation uncertainty and registration failures. This is thus further evidence that the proposed method provides the perfect uncertainty calibration. More results on uncertainty estimations are shown in Fig. E.26 in Appendix.

Despite the promising results, there are some limitations of using σ_f to estimate uncertainty. In this work, we model σ_f as $E[(I_m \circ \phi - I_f)^2]$, which is the MSE of the Monte Carlo sampled registration outputs relative to the fixed image. MSE, on the other hand, is not necessarily the optimal metric for expressing the expected error. In multi-modal registration instances like PET to CT or MRI to CT registration, MSE is anticipated to be high, given the vast difference in image appearance and voxel values across modalities. Thus, if MSE is employed to

quantify uncertainty in these instances, the uncertainty values will be dominated by the squared bias (i.e., $(\hat{I}_f - I_f)^2$ in Eqn. B.3), resulting in an ineffective uncertainty estimate. In these instances, the predicted variance may be a more appropriate choice for uncertainty quantification.

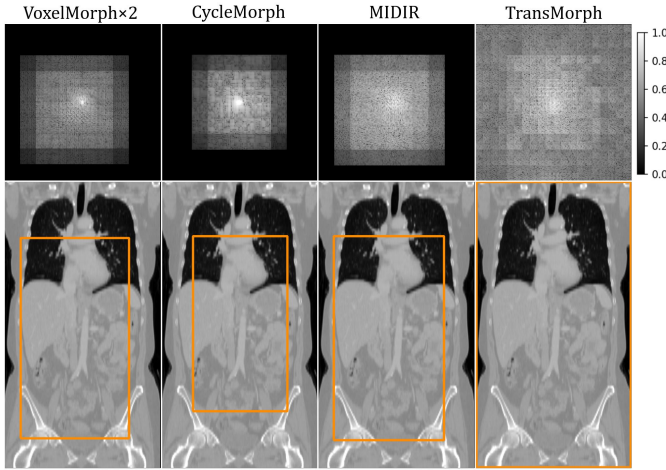


Fig. 16. Example ERFs of the ConvNet-based models and the proposed Transformer-based model TransMorph. The top row shows the center ERF slices (i.e., $y = 80$) on an input image size of $160 \times 160 \times 160$. The non-zero regions of the ERFs are then extracted and interpolated to match the size of the original CT scan. The orange boxes in the bottom row are the delineates the interpolated ERFs on the CT scan.

6.3. Comparison of Effective Receptive Fields

We demonstrate in this section that the *effective receptive fields* (ERFs) of Transformer-based models are larger than that of ConvNet-based models and span the whole spatial domain of an image. We used the definition of ERF introduced in (Luo et al. 2016), which quantifies the amount of influence that each input voxel has on the output of a neural network. In the next paragraph, we briefly discuss the computation of ERF and recommend interested readers to the reference for further information.

Assume the voxels in the input image I_m and the output displacement field \mathbf{u} are indexed by (i, j, k) . We employed an image size of $160 \times 160 \times 160$ (i.e., the size of CT scans used in this work), and the center voxel is located at $(80, 80, 80)$. ERF quantifies how much each $I_m(i, j, k)$ contributes to the center voxel of the displacement field, i.e. $\mathbf{u}(80, 80, 80)$. This is accomplished using the partial derivative $\partial\mathbf{u}(80, 80, 80)/\partial I_m(i, j, k)$, which indicates the relative relevance of $I_m(i, j, k)$ to $\mathbf{u}(80, 80, 80)$. To obtain this partial derivative, we set the error gradient to:

$$\frac{\partial \ell}{\partial \mathbf{u}(i, j, k)} = \begin{cases} 1, & \text{for } (i, j, k) = (80, 80, 80) \\ 0, & \text{otherwise} \end{cases}, \quad (35)$$

where ℓ denotes an arbitrary loss function. Then this gradient is propagated downward from \mathbf{u} to the input I_m , where the resulting gradient of I_m represents the desired partial derivative $\partial\mathbf{u}(80, 80, 80)/\partial I_m(i, j, k)$. This partial derivative is independent of the input and loss function and is only a function of the network architecture and the index (i, j, k) , which adequately describes the distribution of the effective receptive field.

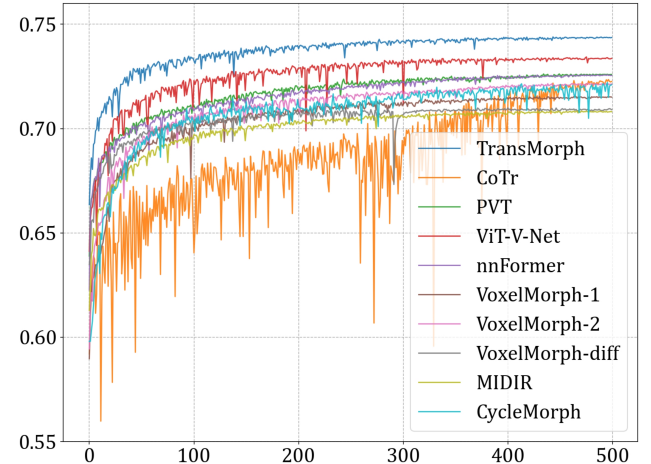


Fig. 17. Validation Dice scores for brain MRI registration during training. The validation dataset comprises 104 image pairings that were not included in the training or testing set.

The comparison of the ERFs of VoxelMorph, CycleMorph, MIDIR, and TransMorph is shown in Fig. 16. Recall that the first three models are built on the ConvNet architecture. Due to the locality of convolution operations, their ERFs (top row in Fig. 16) are small, limited, and square-shaped. On the other hand, the ERF of the proposed TransMorph spans over the entire image. For better visualization, we then extracted the non-zero regions from the ERFs and interpolated their voxel sizes to match that of the original CT scan. The bottom row of Fig. 16 shows the delineation of the interpolated ERFs on top of a CT scan. These figures demonstrate that ConvNet-based architectures can only perceive a portion of the input image, implying that they cannot explicitly comprehend the spatial relationships between distant voxels. Thus, ConvNets may fall short of establishing accurate voxel correspondences between the moving and fixed images, which is essential for image registration. Additionally, since the receptive field of ConvNets only grows with the depth of the layers, the actual receptive fields of the first few layers of ConvNets are even smaller. The proposed TransMorph, on the other hand, sees the entire image at each level of its encoder thanks to the self-attention mechanism of the Transformer.

A full visual comparison of the ERFs of the ConvNet- and Transformer-based models is shown in Fig. F.27 in Appendix.

6.4. Convergence and Speed

Fig. 17 shows the validation dice scores of the learning-based methods during training. In comparison to other methods, the proposed TransMorph achieves > 0.7 in Dice within the first 20 epochs, showing that it learns the spatial correspondence between image pairs quicker than the competing models. Notably, TransMorph consistently outperformed the other Transformer-based models while having a comparable number of parameters and computational complexity. This implies Swin Transformer architecture is more effective than other Transformers, resulting in a performance improvement for TransMorph. On average, Transformer-based models provide better validation scores than

Model	Training (min/epoch)	Inference (sec/image)
SyN	-	192.140
NiftyReg	-	30.723
LDDMM	-	66.829
deedsBCV	-	31.857
VoxelMorph-1	8.75	0.380
VoxelMorph-2	9.40	0.430
VoxelMorph-diff	4.20	0.049
VoxelMorph-huge	28.50	1.107
CycleMorph	41.90	0.281
MIDIR	4.05	1.627
ViT-V-Net	9.20	0.197
PVT	13.80	0.209
CoTr	17.10	0.372
nnFormer	6.35	0.105
TransMorph-Bayes	22.60	7.739
TransMorph-diff	7.35	0.099
TransMorph-bspl	10.50	1.739
TransMorph	14.40	0.329

Table 5. Average training and inference time for methods used in this work. Note that SyN, NiftyReg, and deedsBCV were applied using CPUs, while LDDMM and the learning-based methods were implemented on GPU. Inference time was averaged based on 40 repeated runs.

ConvNet-based models, with the exception of CoTr, whose validation results are volatile during training (as seen from the orange curve in Fig. 17). The performance of CoTr may be limited by its architecture design, which substitutes a Transformer for the skip connections and bottleneck of a U-shaped CovNet. As a result, it lacks the direct flow of features learned during the encoding stage to the layers creating the registration, making it difficult to converge.

Table 5 compares the training and inference time among the methods used in this paper. Note that SyN, NiftyReg, and deedsBCV packages are all CPU-based, while LDDMM and the deep-learning-based methods are all GPU-based. The speed was calculated using an input image size of $160 \times 192 \times 224$, which corresponds to the size of the brain MRI scans. The training time per epoch was computed based on 768 training image pairs. The most and second most time-consuming methods to train are actually two ConvNet-based methods, CycleMorph and the customized VoxelMorph-huge, which required approximately 15 and 10 days for 500 epochs of training, respectively. CycleMorph was time-consuming because the cycle-consistent training virtually trains four networks simultaneously in a single epoch. Whereas the training of VoxelMorph-huge was slowed down by the extensive convolution operations. The proposed TransMorph has a moderate training speed, roughly $1.5 \times$ that of VoxelMorph-2 but $0.5 \times$ that of the customized VoxelMorph-huge. In terms of inference time, learning-based models undoubtedly operated orders of magnitudes faster than traditional registration methods. Among the learning-based models, TransMorph-Bayes required the highest inference time. However, the time required is due to the sampling of $T = 25$ images for a single prediction and uncertainty estimation.

6.5. Limitations

There are some limitations to our work. Rather than doing extensive grid searches for optimal hyper-parameters for base-

line methods, the hyper-parameters are either determined empirically or based on the values suggested in the original paper. Due to the time required to train some of the baseline methods and limited by the memory available on the GPU, we were unable to afford the intensive grid search. Since this paper introduced a generic network architecture for image registration, we concentrated on architectural comparison rather than selecting optimal hyper-parameters for loss functions or advanced training methods. However, the proposed TransMorph architecture is readily adaptable to various training methods, such as the cycle-consistent training used by CycleMorph (Kim *et al.* 2021) or the symmetric training proposed in (Mok and Chung 2020). Additionally, the proposed model may be used in conjunction with any registration loss function.

In the future, we will continue to analyze TransMorph on publicly available datasets. Furthermore, we will investigate alternative loss functions, such as mutual information, in an effort to expand the potential of the proposed method for multi-modal registration tasks.

7. Conclusion

In this paper, we introduced TransMorph, a novel model for unsupervised deformable image registration. TransMorph is built on Transformer, which is well-known for its capability to establish long-range spatial correspondence between image voxels, making TransMorph a strong candidate for image registration tasks.

Two variants of TransMorph are proposed, which provide topology-preserved deformations. Additionally, we introduced Bayesian deep learning to the Transformer encoder of TransMorph, enabling deformation uncertainty estimation without degrading registration performance.

We evaluated TransMorph on the task of inter-patient brain MR registration and a novel task of phantom-to-CT registration. The results revealed that TransMorph achieved superior registration accuracy than various traditional and learning-based methods, demonstrating its effectiveness for medical image registration.

Acknowledgments

This work was supported by a grant from the National Cancer Institute, U01-CA140204. The views expressed in written conference materials or publications and by speakers and moderators do not necessarily reflect the official policies of the NIH; nor does mention by trade names, commercial practices, or organizations imply endorsement by the U.S. Government.

Appendix

Appendix A. Affine Network Architecture

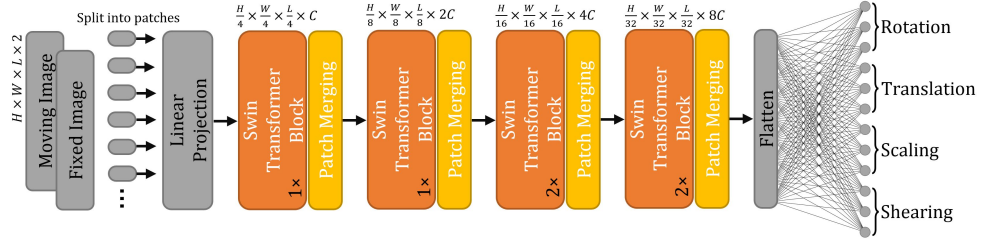


Fig. A.18. Visualization of the proposed Swin-Transformer-based affine network. This network outputs three rotation, three translation, three scaling, and three shearing parameters for rigid registration. The embedding dimension C in the network was set to 12.

Appendix B. Miscalibration in Predictive Variance

The expected model error (characterized by MSE) is defined as:

$$err(I_m \circ \phi) = \mathbb{E}[(I_m \circ \phi - I_f)^2] = \frac{1}{T} \sum_{t=1}^T (I_m \circ \phi_t - I_f)^2, \quad (\text{B.1})$$

where t represents the t^{th} sample from a total number of T samples. We denote $I_d = I_m \circ \phi$ for convenience, and it can be shown that:

$$\begin{aligned} \mathbb{E}[(I_d - I_f)^2] &= \mathbb{E}[(I_d - \mathbb{E}[I_d] + \mathbb{E}[I_d] - I_f)^2] \\ &= \mathbb{E}[(I_d - \mathbb{E}[I_d])^2] + (\mathbb{E}[I_d] - I_f)^2 + 2(\mathbb{E}[I_d] - I_f)\mathbb{E}[I_d - \mathbb{E}[I_d]] \\ &= \mathbb{E}[(I_d - \mathbb{E}[I_d])^2] + (\mathbb{E}[I_d] - I_f)^2. \end{aligned} \quad (\text{B.2})$$

Therefore,

$$\begin{aligned} err(I_m \circ \phi) &= \frac{1}{T} \sum_{t=1}^T (I_m \circ \phi_t - I_f)^2 \\ &= \frac{1}{T} \sum_{t=1}^T \left(I_m \circ \phi_t - \frac{1}{T} \sum_{t=1}^T I_m \circ \phi_t \right)^2 + \left(\frac{1}{T} \sum_{t=1}^T I_m \circ \phi_t - I_f \right)^2 \\ &= \hat{\Sigma}_f^2 + (\hat{I}_f - I_f)^2, \end{aligned} \quad (\text{B.3})$$

where $\hat{I}_f - I_f$ is referred to as the bias between the predictive mean \hat{I}_f and the target image I_f . Due to the problem of overfitting the training set in supervised algorithms (e.g., deep learning) (Bishop 2006), this bias may be less noticeable on training dataset but more noticeable on test images, which is a phenomenon referred to as the *bias-variance tradeoff* (Friedman 2017). As a consequence, the predictive variance $\hat{\Sigma}_f^2$ is systematically smaller than the expected error $err(I_m \circ \phi)$, resulting in miscalibrated uncertainty estimations.

Appendix C. Additional Results for Inter-patient Brain MRI Registration

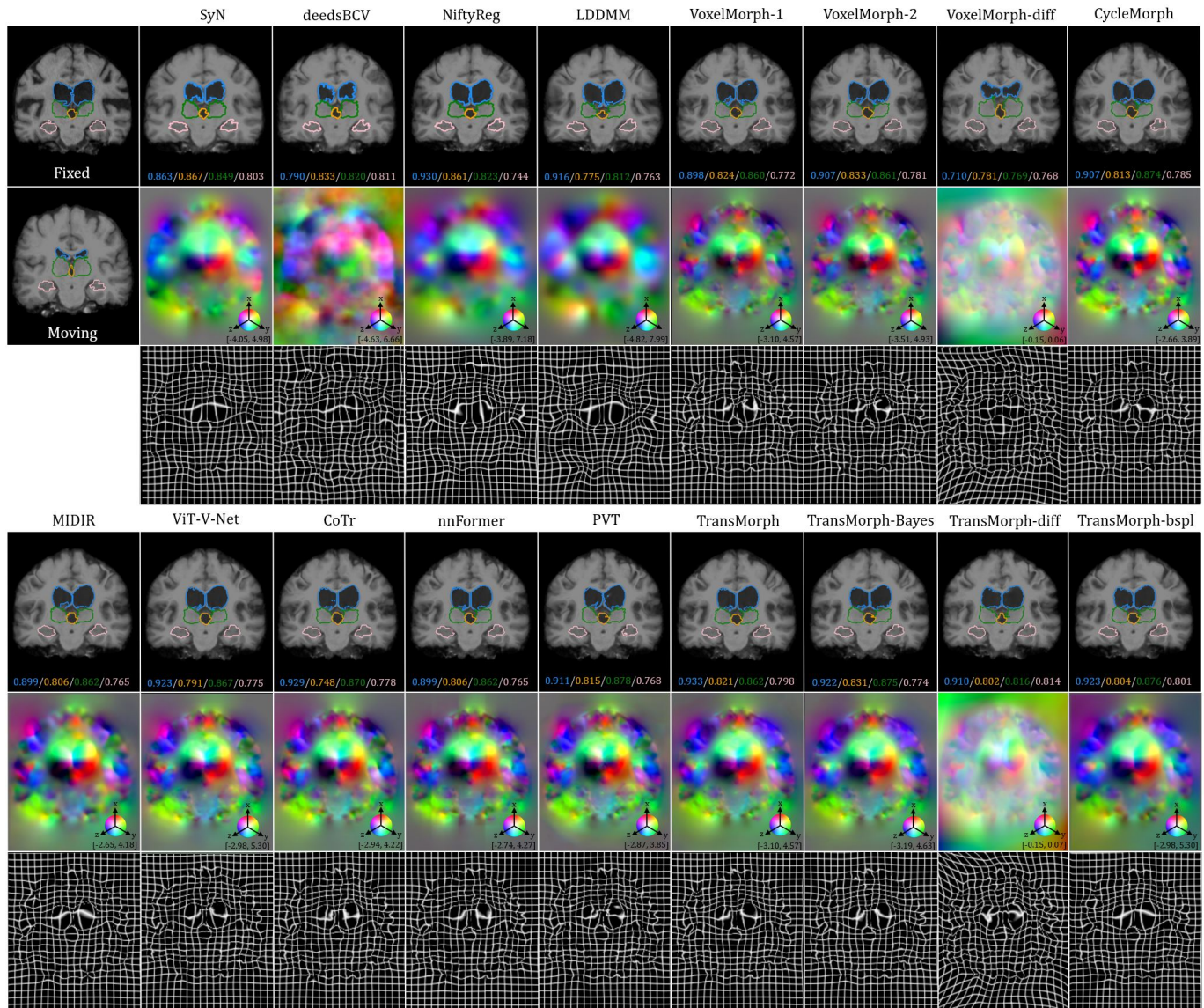


Fig. C.19. Additional qualitative comparison of various registration methods on brain MR registration. The first row shows the deformed moving images, the second row shows the deformation fields, and the last row shows the deformed grids.

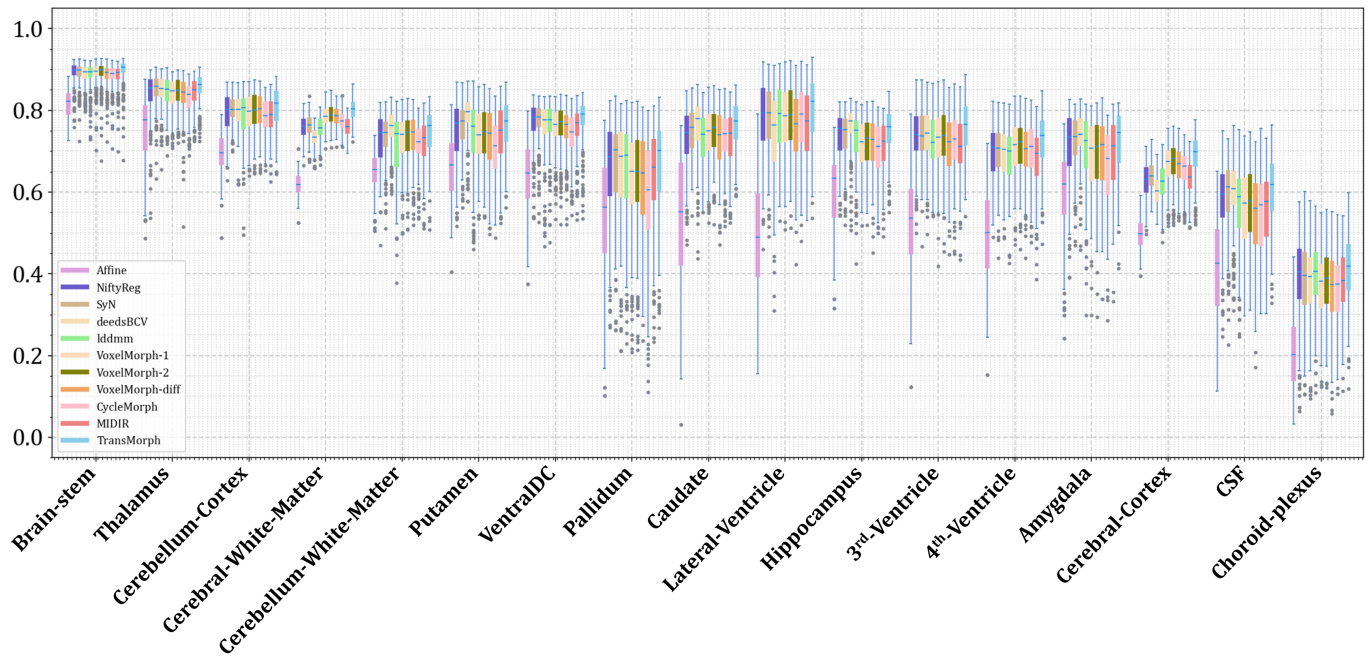


Fig. C.20. Boxplots showing Dice scores for different brain MR substructures using the proposed TransMorph and existing image registration methods.

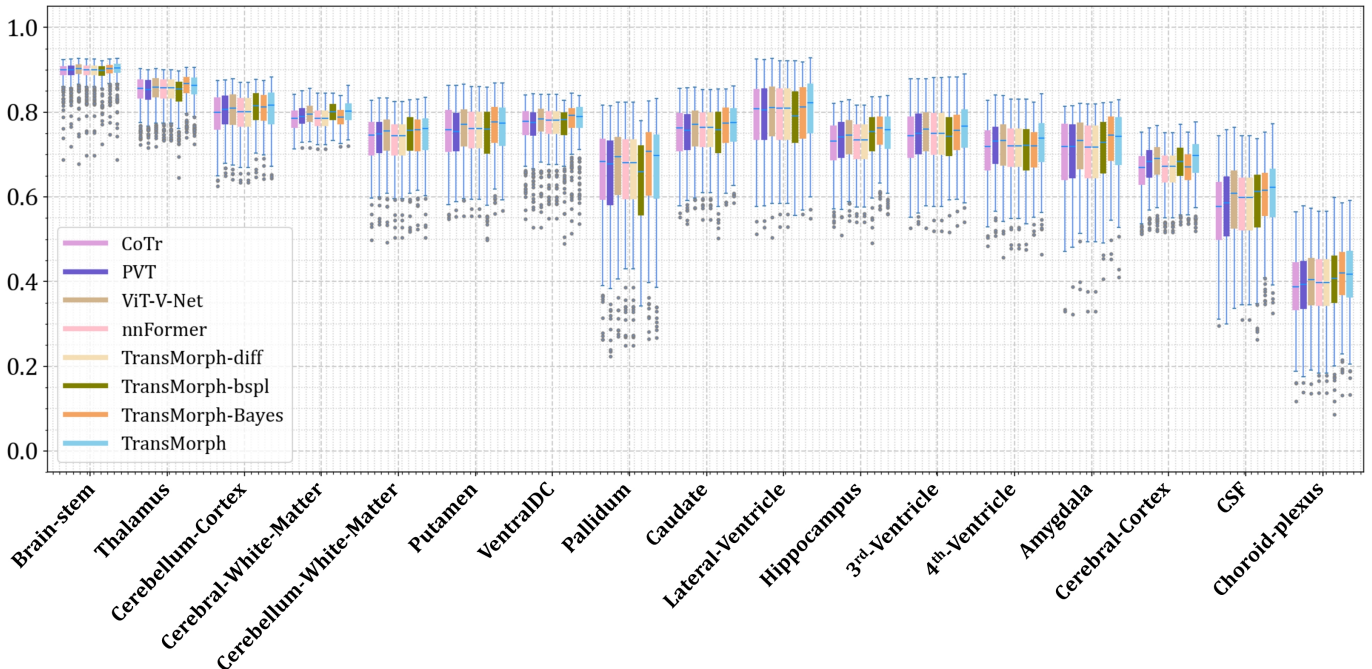


Fig. C.21. Boxplots showing Dice scores for different brain MR substructures using the proposed TransMorph, the variants of TransMorph, and other Transformer architectures.

Appendix D. Additional Results for XCAT-to-CT Registration

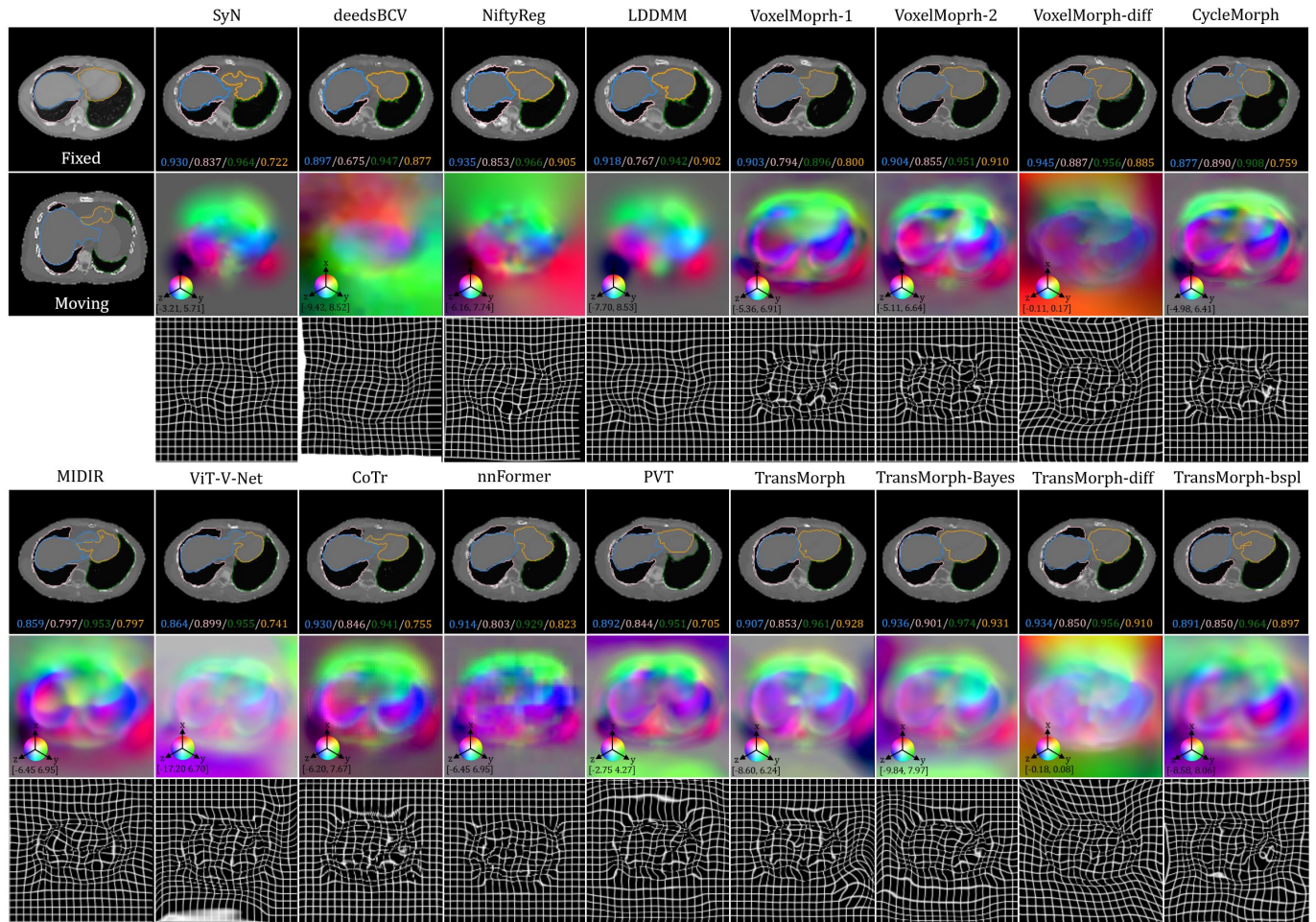


Fig. D.22. Additional qualitative comparison of various registration methods on XCAT-to-CT registration. The first row shows the deformed moving images, the second row shows the deformation fields, and the last row shows the deformed grids.

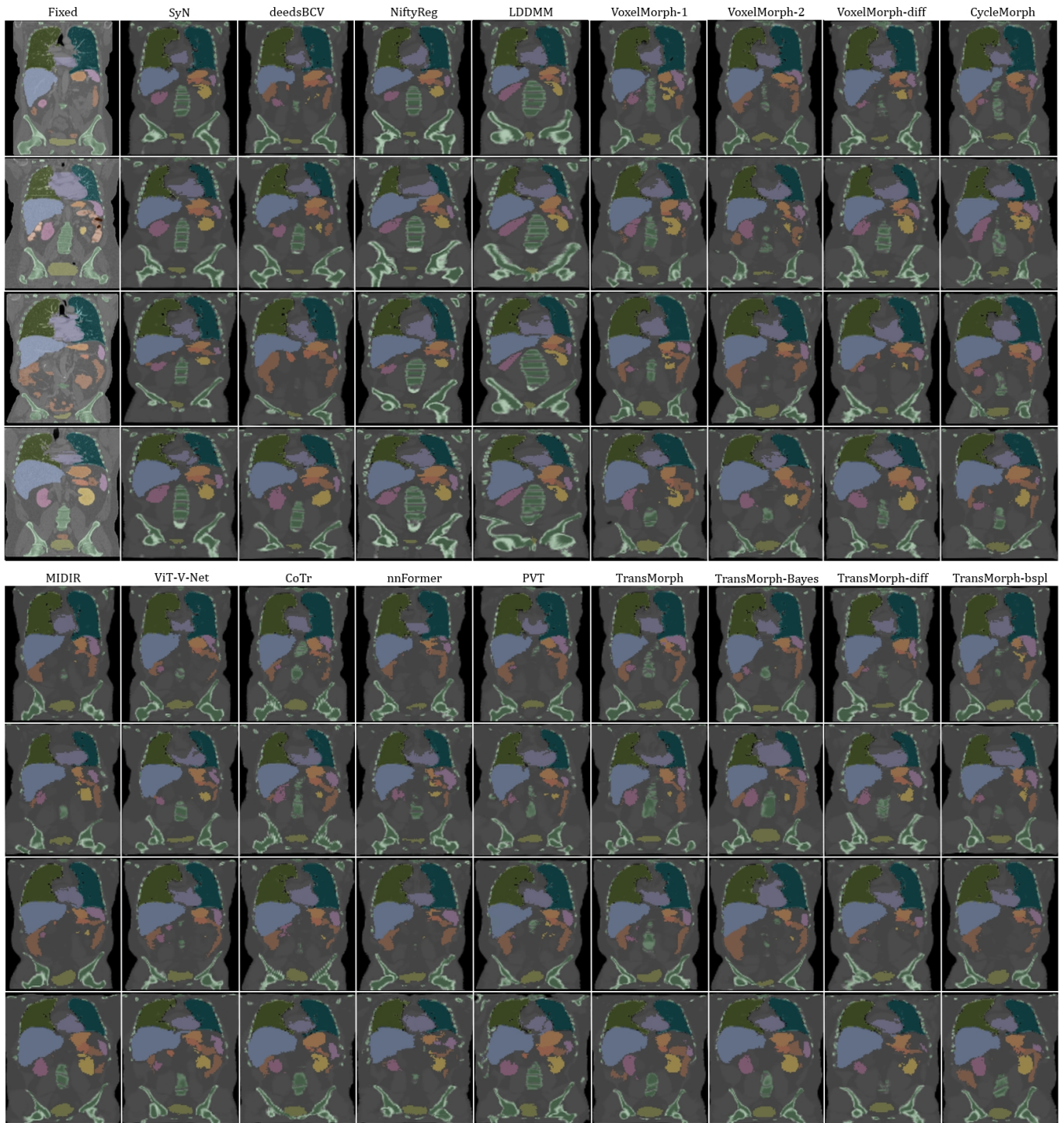


Fig. D.23. Additional coronal slices of the deformed XCAT phantom generated by various registration methods.

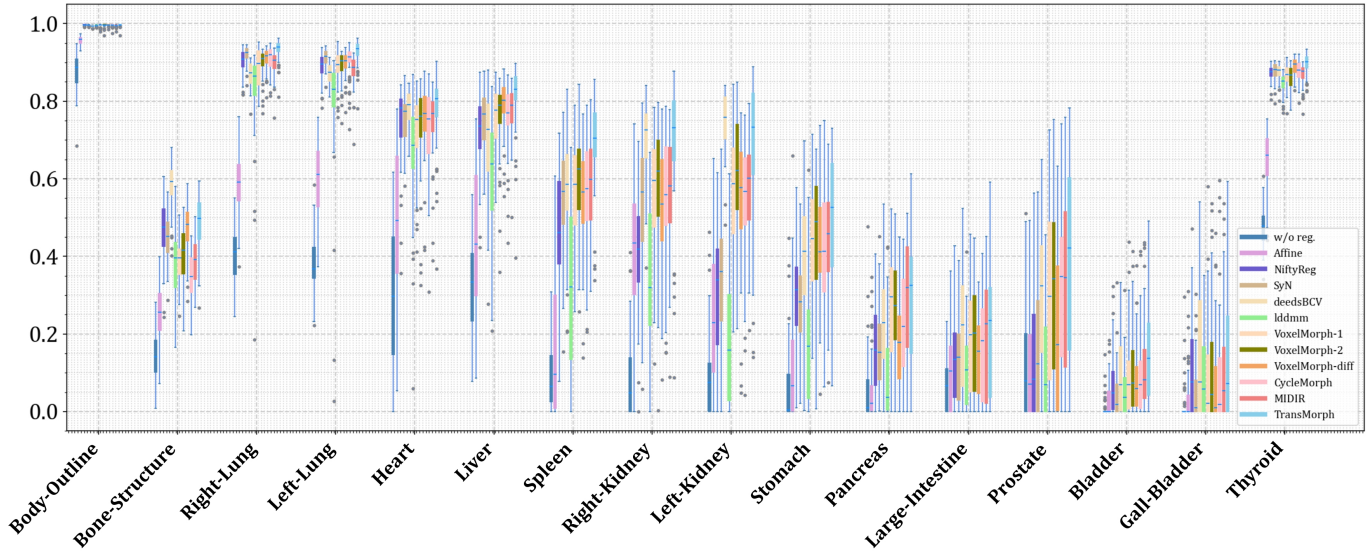


Fig. D.24. Boxplots showing Dice scores for different organs in CT obtained using the proposed TransMorph and existing image registration methods.

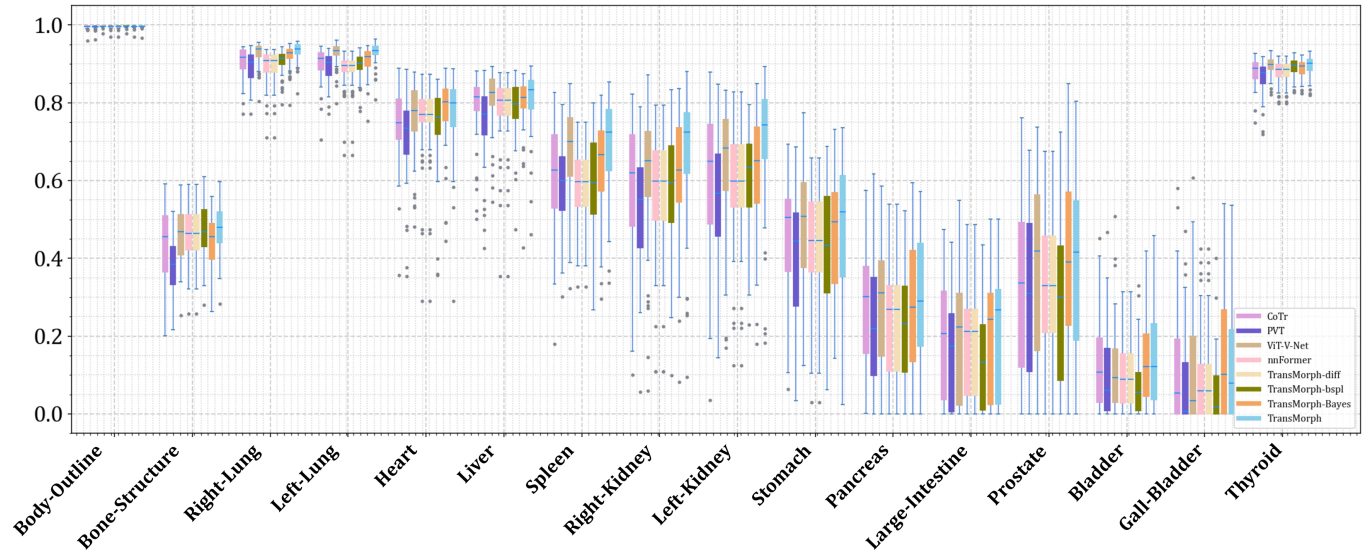


Fig. D.25. Boxplots showing Dice scores for different organs in CT obtained using the proposed TransMorph, the variants of TransMorph, and other Transformer architectures.

Appendix E. Additional Qualitative Results for Uncertainty Quantification

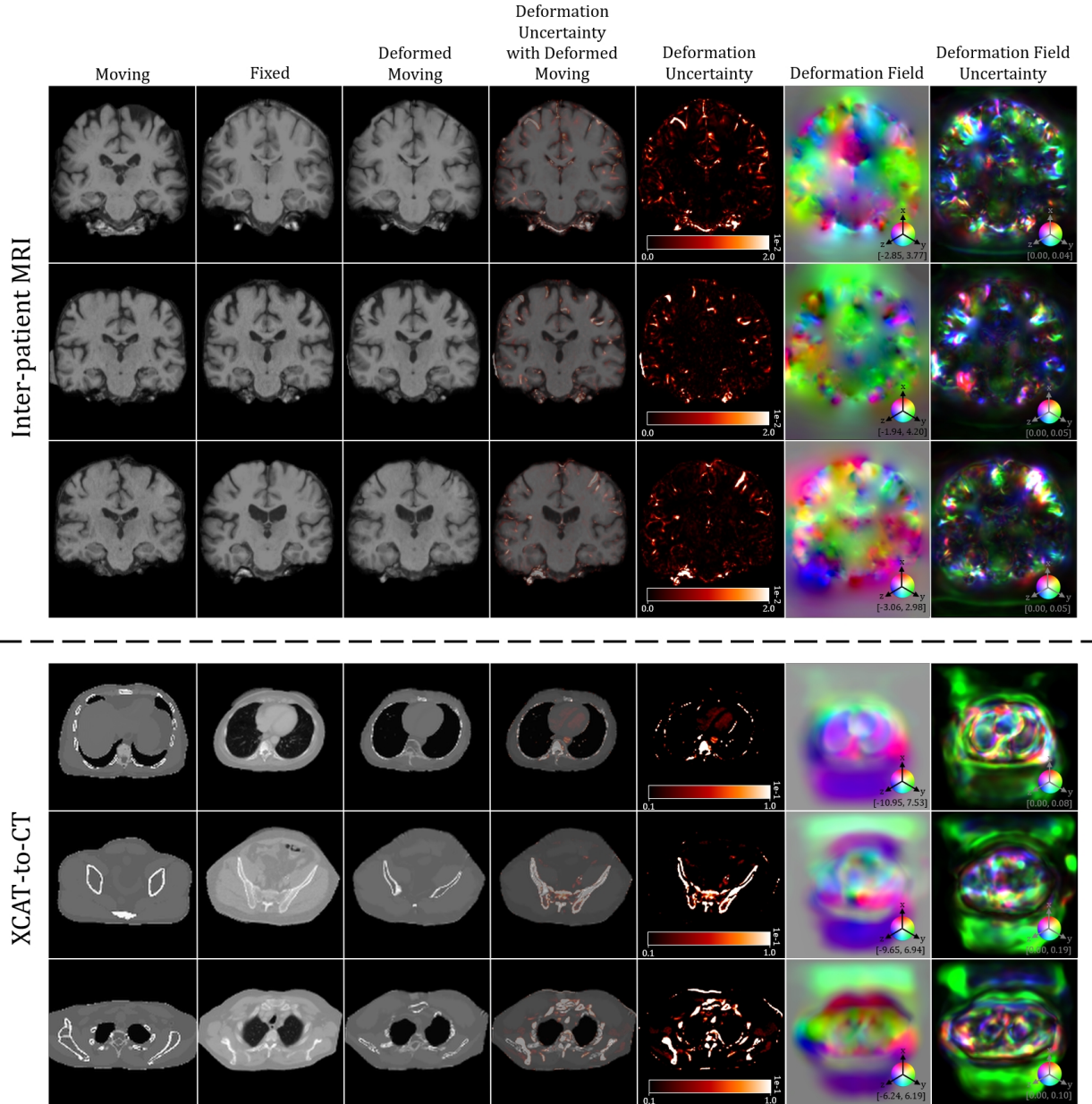


Fig. E.26. Qualitative results and registration uncertainty estimate with TransMorph-Bayes. The fourth and the fifth columns exhibit the registration uncertainties estimated using the proposed uncertainty estimation scheme (i.e., Σ^2). The last column shows the uncertainties in the deformation fields. Since the target deformation fields are inaccessible, the uncertainties in the deformation fields were estimated using $\hat{\Sigma}^2$.

Appendix F. Visual Comparison of Effective Receptive Fields

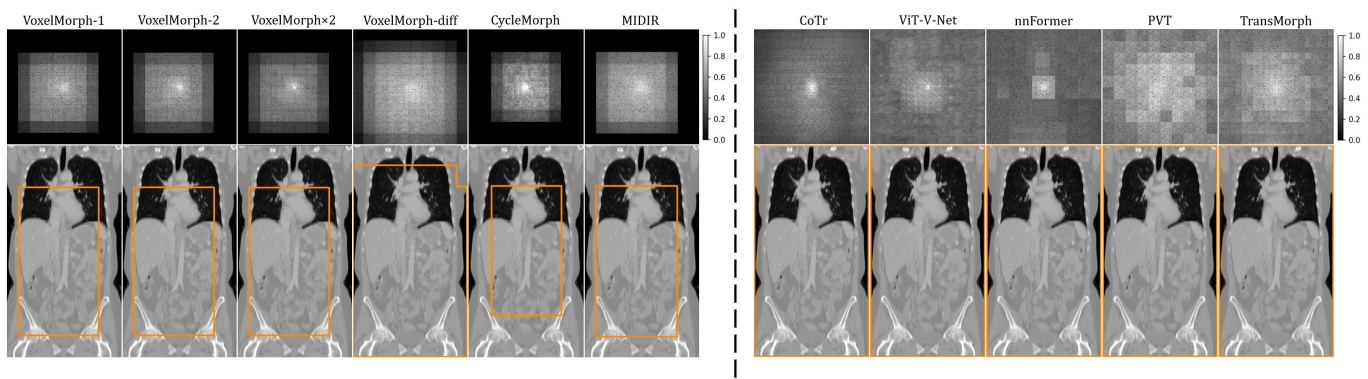


Fig. F.27. Comparison of the effective receptive fields (ERFs) of different neural network architecture after training. The Transformer-based models (i.e., TransMorph, CoTr, PVT, and nnFormer) exhibit large ERFs that covers the entire image domain. The ConvNet-based models, however, have small rectangular ERFs which are limited by the convolution operations.

Appendix G. Visualization of Feature Maps in Skip Connections

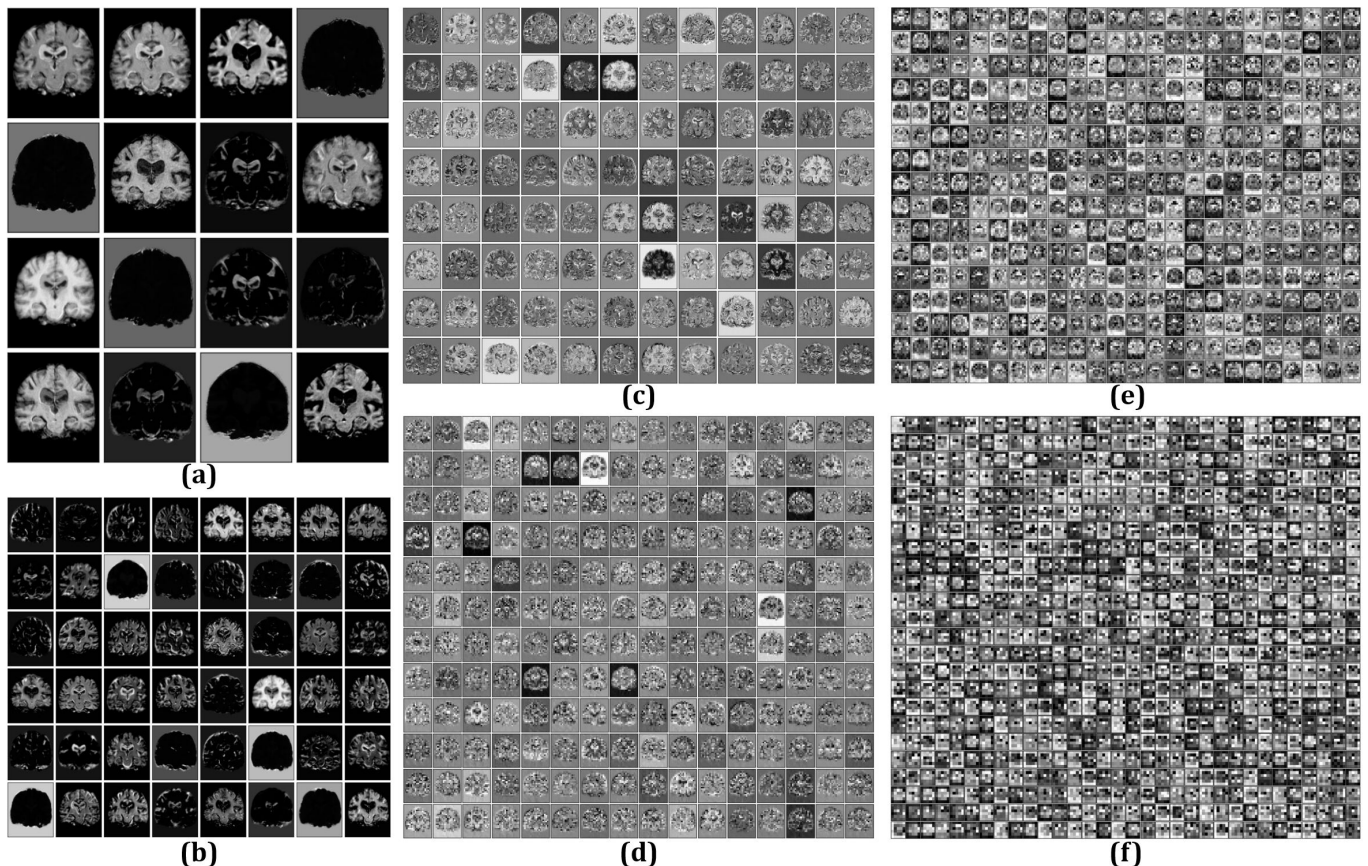


Fig. G.28. Feature maps in TransMorph's skip connections. (a) and (b) exhibit, respectively, the feature maps in the first and second skip connections from the convolutional layers in the encoder (i.e., the green arrows in Fig. 2); (c)-(f) exhibit the feature maps in the skip connections from the Transformer blocks (i.e., the orange arrows in Fig. 2).

References

- Alom, M.Z., Hasan, M., Yakopcic, C., Taha, T.M., Asari, V.K., 2018. Recurrent residual convolutional neural network based on u-net (r2u-net) for medical image segmentation. arXiv preprint arXiv:1802.06955.
- Arsigny, V., Commowick, O., Pennec, X., Ayache, N., 2006. A log-euclidean framework for statistics on diffeomorphisms, in: International Conference on Medical Image Computing and Computer-Assisted Intervention, Springer. pp. 924–931.
- Atanov, A., Ashukha, A., Molchanov, D., Neklyudov, K., Vetrov, D., 2018. Uncertainty estimation via stochastic batch normalization. arXiv preprint arXiv:1802.04893.
- Avants, B.B., Epstein, C.L., Grossman, M., Gee, J.C., 2008. Symmetric diffeomorphic image registration with cross-correlation: evaluating automated labeling of elderly and neurodegenerative brain. Medical image analysis 12, 26–41.
- Balakrishnan, G., Zhao, A., Sabuncu, M.R., Guttag, J., Dalca, A.V., 2018. An unsupervised learning model for deformable medical image registration, in: Proceedings of the IEEE conference on computer vision and pattern recognition, pp. 9252–9260.
- Balakrishnan, G., Zhao, A., Sabuncu, M.R., Guttag, J., Dalca, A.V., 2019. Voxelmorph: a learning framework for deformable medical image registration. IEEE transactions on medical imaging 38, 1788–1800.
- Baumgartner, C.F., Tezcan, K.C., Chaitanya, K., Hötker, A.M., Muehlematter, U.J., Schawkat, K., Becker, A.S., Donati, O., Konukoglu, E., 2019. Phiseg: Capturing uncertainty in medical image segmentation, in: International Conference on Medical Image Computing and Computer-Assisted Intervention, Springer. pp. 119–127.
- Beg, M.F., Miller, M.I., Trouvé, A., Younes, L., 2005. Computing large deformation metric mappings via geodesic flows of diffeomorphisms. International journal of computer vision 61, 139–157.
- Bishop, C.M., 2006. Pattern recognition. Machine learning 128.
- Blundell, C., Cornebise, J., Kavukcuoglu, K., Wierstra, D., 2015. Weight uncertainty in neural network, in: International Conference on Machine Learning, PMLR. pp. 1613–1622.
- Cao, X., Yang, J., Wang, L., Xue, Z., Wang, Q., Shen, D., 2018. Deep learning based inter-modality image registration supervised by intra-modality similarity, in: International workshop on machine learning in medical imaging, Springer. pp. 55–63.
- Chen, J., He, Y., Frey, E.C., Li, Y., Du, Y., 2021a. Vit-v-net: Vision transformer for unsupervised volumetric medical image registration. arXiv preprint arXiv:2104.06468.
- Chen, J., Jha, A.K., Frey, E.C., 2019. Incorporating ct prior information in the robust fuzzy c-means algorithm for qspect image segmentation, in: Medical Imaging 2019: Image Processing, International Society for Optics and Photonics. p. 109491W.
- Chen, J., Li, Y., Du, Y., Frey, E.C., 2020. Generating anthropomorphic phantoms using fully unsupervised deformable image registration with convolutional neural networks. Medical physics .
- Chen, J., Lu, Y., Yu, Q., Luo, X., Adeli, E., Wang, Y., Lu, L., Yuille, A.L., Zhou, Y., 2021b. Transunet: Transformers make strong encoders for medical image segmentation. arXiv preprint arXiv:2102.04306.
- Christoffersen, C.P., Hansen, D., Poulsen, P., Sorensen, T.S., 2013. Registration-based reconstruction of four-dimensional cone beam computed tomography. IEEE Transactions on Medical Imaging 32, 2064–2077. doi:10.1109/TMI.2013.2272882.
- Cui, K., Fu, P., Li, Y., Lin, Y., 2021. Bayesian fully convolutional networks for brain image registration. Journal of Healthcare Engineering 2021.
- Dai, X., Chen, Y., Xiao, B., Chen, D., Liu, M., Yuan, L., Zhang, L., 2021. Dynamic head: Unifying object detection heads with attentions, in: Proceedings of the IEEE/CVF Conference on Computer Vision and Pattern Recognition, pp. 7373–7382.
- Dalca, A.V., Balakrishnan, G., Guttag, J., Sabuncu, M.R., 2019. Unsupervised learning of probabilistic diffeomorphic registration for images and surfaces. Medical image analysis 57, 226–236.
- Devalla, S.K., Renukanand, P.K., Sreedhar, B.K., Subramanian, G., Zhang, L., Perera, S., Mari, J.M., Chin, K.S., Tun, T.A., Strouthidis, N.G., et al., 2018. Drunet: a dilated-residual u-net deep learning network to segment optic nerve head tissues in optical coherence tomography images. Biomedical optics express 9, 3244–3265.
- DeVries, T., Taylor, G.W., 2018. Leveraging uncertainty estimates for predicting segmentation quality. arXiv preprint arXiv:1807.00502.
- Dice, L.R., 1945. Measures of the amount of ecologic association between species. Ecology 26, 297–302.
- Dong, X., Bao, J., Chen, D., Zhang, W., Yu, N., Yuan, L., Chen, D., Guo, B., 2021. Cswin transformer: A general vision transformer backbone with cross-shaped windows. arXiv preprint arXiv:2107.00652.
- Dosovitskiy, A., Beyer, L., Kolesnikov, A., Weissenborn, D., Zhai, X., Unterthiner, T., Dehghani, M., Minderer, M., Heigold, G., Gelly, S., et al., 2020. An image is worth 16x16 words: Transformers for image recognition at scale. arXiv preprint arXiv:2010.11929 .
- Fischl, B., 2012. Freesurfer. Neuroimage 62, 774–781.
- Friedman, J.H., 2017. The elements of statistical learning: Data mining, inference, and prediction. Springer open.
- Fu, W., Sharma, S., Abadi, E., Iliopoulos, A.S., Wang, Q., Sun, X., Lo, J.Y.C., Segars, W.P., Samei, E., 2021. iphantom: a framework for automated creation of individualized computational phantoms and its application to ct organ dosimetry. IEEE Journal of Biomedical and Health Informatics .
- Gal, Y., Ghahramani, Z., 2016. Dropout as a bayesian approximation: Representing model uncertainty in deep learning, in: international conference on machine learning, PMLR. pp. 1050–1059.
- Guo, C., Pleiss, G., Sun, Y., Weinberger, K.Q., 2017. On calibration of modern neural networks, in: International Conference on Machine Learning, PMLR. pp. 1321–1330.
- He, K., Zhang, X., Ren, S., Sun, J., 2016. Deep residual learning for image recognition, in: Proceedings of the IEEE conference on computer vision and pattern recognition, pp. 770–778.
- Heinrich, M.P., Jenkinson, M., Brady, M., Schnabel, J.A., 2013a. Mrf-based deformable registration and ventilation estimation of lung ct. IEEE transactions on medical imaging 32, 1239–1248.
- Heinrich, M.P., Jenkinson, M., Papiez, B.W., Brady, M., Schnabel, J.A., 2013b. Towards realtime multimodal fusion for image-guided interventions using self-similarities, in: International conference on medical image computing and computer-assisted intervention, Springer. pp. 187–194.
- Heinrich, M.P., Maier, O., Handels, H., 2015. Multi-modal multi-atlas segmentation using discrete optimisation and self-similarities. VISCERAL Challenge@ ISBI 1390, 27.
- Hoffmann, M., Billot, B., Iglesias, J.E., Fischl, B., Dalca, A.V., 2020. Learning image registration without images. arXiv preprint arXiv:2004.10282 .
- Isensee, F., Jaeger, P.F., Kohl, S.A., Petersen, J., Maier-Hein, K.H., 2021. nnunet: a self-configuring method for deep learning-based biomedical image segmentation. Nature methods 18, 203–211.
- Jaderberg, M., Simonyan, K., Zisserman, A., et al., 2015. Spatial transformer networks. Advances in neural information processing systems 28, 2017–2025.
- Jha, D., Smedsrød, P.H., Riegler, M.A., Johansen, D., De Lange, T., Halvorsen, P., Johansen, H.D., 2019. Resunet++: An advanced architecture for medical image segmentation, in: 2019 IEEE International Symposium on Multimedia (ISM), IEEE. pp. 225–2255.
- Johnson, H.J., Christensen, G.E., 2002. Consistent landmark and intensity-based image registration. IEEE transactions on medical imaging 21, 450–461.
- Kendall, A., Gal, Y., 2017. What uncertainties do we need in Bayesian deep learning for computer vision?, in: Advances in Neural Information Processing Systems, Neural information processing systems foundation. pp. 5575–5585. URL: <https://arxiv.org/abs/1703.04977v2>, arXiv:1703.04977.
- Kim, B., Kim, D.H., Park, S.H., Kim, J., Lee, J.G., Ye, J.C., 2021. Cyclemorph: Cycle consistent unsupervised deformable image registration. Medical Image Analysis 71, 102036.
- Kingma, D.P., Welling, M., 2013. Auto-encoding variational bayes. arXiv preprint arXiv:1312.6114 .
- Krebs, J., Delingette, H., Mailh  , B., Ayache, N., Mansi, T., 2019. Learning a probabilistic model for diffeomorphic registration. IEEE transactions on medical imaging 38, 2165–2176.
- Kuleshov, V., Fenner, N., Ermon, S., 2018. Accurate uncertainties for deep learning using calibrated regression, in: International Conference on Machine Learning, PMLR. pp. 2796–2804.
- Kyb  , J., 2009. Bootstrap resampling for image registration uncertainty estimation without ground truth. IEEE Transactions on Image Processing 19, 64–73.
- Laves, M.H., Ihler, S., Fast, J.F., Kahrs, L.A., Ortmaier, T., 2020a. Well-calibrated regression uncertainty in medical imaging with deep learning, in: Arbel, T., Ben Ayed, I., de Bruijne, M., Descoteaux, M., Lombaert, H., Pal,

- C. (Eds.), Proceedings of the Third Conference on Medical Imaging with Deep Learning, PMLR, pp. 393–412. URL: <https://proceedings.mlr.press/v121/laves20a.html>.
- Laves, M.H., Ihler, S., Kortmann, K.P., Ortmaier, T., 2019. Well-calibrated model uncertainty with temperature scaling for dropout variational inference. arXiv preprint arXiv:1909.13550.
- Laves, M.H., Tölle, M., Ortmaier, T., 2020b. Uncertainty Estimation in Medical Image Denoising with Bayesian Deep Image Prior. Lecture Notes in Computer Science (including subseries Lecture Notes in Artificial Intelligence and Lecture Notes in Bioinformatics) 12443 LNCS, 81–96. URL: <https://arxiv.org/abs/2008.08837v1>, arXiv:2008.08837.
- Laves, M.H., Tölle, M., Ortmaier, T., 2020c. Uncertainty estimation in medical image denoising with bayesian deep image prior, in: Uncertainty for Safe Utilization of Machine Learning in Medical Imaging, and Graphs in Biomedical Image Analysis. Springer, pp. 81–96.
- Lei, Y., Fu, Y., Wang, T., Liu, Y., Patel, P., Curran, W.J., Liu, T., Yang, X., 2020. 4d-ct deformable image registration using multiscale unsupervised deep learning. Physics in Medicine & Biology 65, 085003.
- Levi, D., Gispan, L., Giladi, N., Fetaya, E., 2019. Evaluating and calibrating uncertainty prediction in regression tasks. arXiv preprint arXiv:1905.11659.
- Li, S., Sui, X., Luo, X., Xu, X., Liu, Y., Goh, R.S.M., 2021. Medical image segmentation using squeeze-and-expansion transformers. arXiv preprint arXiv:2105.09511.
- Lian, C., Liu, M., Zhang, J., Shen, D., 2018. Hierarchical fully convolutional network for joint atrophy localization and alzheimer’s disease diagnosis using structural mri. IEEE transactions on pattern analysis and machine intelligence 42, 880–893.
- Liu, Z., Lin, Y., Cao, Y., Hu, H., Wei, Y., Zhang, Z., Lin, S., Guo, B., 2021a. Swin transformer: Hierarchical vision transformer using shifted windows. arXiv preprint arXiv:2103.14030.
- Liu, Z., Ning, J., Cao, Y., Wei, Y., Zhang, Z., Lin, S., Hu, H., 2021b. Video swin transformer. arXiv preprint arXiv:2106.13230.
- Long, J., Shelhamer, E., Darrell, T., 2015. Fully convolutional networks for semantic segmentation, in: Proceedings of the IEEE conference on computer vision and pattern recognition, pp. 3431–3440.
- Luo, J., Sedghi, A., Popuri, K., Cobzas, D., Zhang, M., Preiswerk, F., Toews, M., Golby, A., Sugiyama, M., Wells, W.M., et al., 2019. On the applicability of registration uncertainty, in: International Conference on Medical Image Computing and Computer-Assisted Intervention, Springer, pp. 410–419.
- Luo, W., Li, Y., Urtasun, R., Zemel, R., 2016. Understanding the effective receptive field in deep convolutional neural networks, in: Proceedings of the 30th International Conference on Neural Information Processing Systems, pp. 4905–4913.
- Maas, A.L., Hannun, A.Y., Ng, A.Y., et al., 2013. Rectifier nonlinearities improve neural network acoustic models, in: Proc. icml, Citeseer, p. 3.
- Mehrtash, A., Wells, W.M., Tempany, C.M., Abolmaesumi, P., Kapur, T., 2020. Confidence calibration and predictive uncertainty estimation for deep medical image segmentation. IEEE transactions on medical imaging 39, 3868–3878.
- Milletari, F., Navab, N., Ahmadi, S.A., 2016. V-net: Fully convolutional neural networks for volumetric medical image segmentation, in: 2016 fourth international conference on 3D vision (3DV), IEEE, pp. 565–571.
- Modat, M., Ridgway, G.R., Taylor, Z.A., Lehmann, M., Barnes, J., Hawkes, D.J., Fox, N.C., Ourselin, S., 2010. Fast free-form deformation using graphics processing units. Computer methods and programs in biomedicine 98, 278–284.
- Mok, T.C., Chung, A., 2020. Fast symmetric diffeomorphic image registration with convolutional neural networks, in: Proceedings of the IEEE/CVF conference on computer vision and pattern recognition, pp. 4644–4653.
- Niethammer, M., Kwitt, R., Vialard, F.X., 2019. Metric learning for image registration, in: Proceedings of the IEEE/CVF Conference on Computer Vision and Pattern Recognition, pp. 8463–8472.
- Onofrey, J.A., Staib, L.H., Papademetris, X., 2013. Semi-supervised learning of nonrigid deformations for image registration, in: International MICCAI Workshop on Medical Computer Vision, Springer, pp. 13–23.
- Pace, D.F., Aylward, S.R., Niethammer, M., 2013. A locally adaptive regularization based on anisotropic diffusion for deformable image registration of sliding organs. IEEE transactions on medical imaging 32, 2114–2126.
- Paszke, A., Gross, S., Massa, F., Lerer, A., Bradbury, J., Chanan, G., Killeen, T., Lin, Z., Gimelshein, N., Antiga, L., et al., 2019. Pytorch: An imperative style, high-performance deep learning library. Advances in neural information processing systems 32, 8026–8037.
- Phan, B., Salay, R., Czarnecki, K., Abdelzad, V., Denouden, T., Vernekar, S., 2018. Calibrating uncertainties in object localization task. arXiv preprint arXiv:1811.11210.
- Qiu, H., Qin, C., Schuh, A., Hammernik, K., Rueckert, D., 2021. Learning diffeomorphic and modality-invariant registration using b-splines, in: Medical Imaging with Deep Learning.
- Raghu, M., Unterthiner, T., Kornblith, S., Zhang, C., Dosovitskiy, A., 2021. Do vision transformers see like convolutional neural networks? arXiv preprint arXiv:2108.08810.
- Redmon, J., Divvala, S., Girshick, R., Farhadi, A., 2016. You only look once: Unified, real-time object detection, in: Proceedings of the IEEE conference on computer vision and pattern recognition, pp. 779–788.
- Risholm, P., Balter, J., Wells, W.M., 2011. Estimation of delivered dose in radiotherapy: the influence of registration uncertainty, in: International Conference on Medical Image Computing and Computer-Assisted Intervention, Springer, pp. 548–555.
- Risholm, P., Janoos, F., Norton, I., Golby, A.J., Wells III, W.M., 2013. Bayesian characterization of uncertainty in intra-subject non-rigid registration. Medical image analysis 17, 538–555.
- Rohé, M.M., Datar, M., Heimann, T., Sermesant, M., Pennec, X., 2017. Svfnet: Learning deformable image registration using shape matching, in: International conference on medical image computing and computer-assisted intervention, Springer, pp. 266–274.
- Ronneberger, O., Fischer, P., Brox, T., 2015. U-net: Convolutional networks for biomedical image segmentation, in: International Conference on Medical image computing and computer-assisted intervention, Springer, pp. 234–241.
- Rueckert, D., Sonoda, L.I., Hayes, C., Hill, D.L., Leach, M.O., Hawkes, D.J., 1999. Nonrigid registration using free-form deformations: application to breast mr images. IEEE transactions on medical imaging 18, 712–721.
- Sedghi, A., Kapur, T., Luo, J., Mousavi, P., Wells, W.M., 2019. Probabilistic image registration via deep multi-class classification: characterizing uncertainty, in: Uncertainty for Safe Utilization of Machine Learning in Medical Imaging and Clinical Image-Based Procedures. Springer, pp. 12–22.
- Segars, W., Bond, J., Frush, J., Hon, S., Eckersley, C., Williams, C.H., Feng, J., Tward, D.J., Ratnanather, J., Miller, M., et al., 2013. Population of anatomically variable 4d xcat adult phantoms for imaging research and optimization. Medical physics 40, 043701.
- Segars, W.P., Sturgeon, G., Mendonca, S., Grimes, J., Tsui, B.M., 2010. 4d xcat phantom for multimodality imaging research. Medical physics 37, 4902–4915.
- Sentker, T., Madesta, F., Werner, R., 2018. Gdl-fire4d: Deep learning-based fast 4d ct image registration, in: International Conference on Medical Image Computing and Computer-Assisted Intervention, Springer, pp. 765–773.
- Shen, Z., Han, X., Xu, Z., Niethammer, M., 2019. Networks for joint affine and non-parametric image registration, in: Proceedings of the IEEE/CVF Conference on Computer Vision and Pattern Recognition, pp. 4224–4233.
- Simpson, I.J., Woolrich, M., Groves, A.R., Schnabel, J.A., 2011. Longitudinal brain mri analysis with uncertain registration, in: International Conference on Medical Image Computing and Computer-Assisted Intervention, Springer, pp. 647–654.
- Sokooti, H., De Vos, B., Berendsen, F., Lelieveldt, B.P., Isgum, I., Staring, M., 2017. Nonrigid image registration using multi-scale 3d convolutional neural networks, in: International conference on medical image computing and computer-assisted intervention, Springer, pp. 232–239.
- Srivastava, N., Hinton, G., Krizhevsky, A., Sutskever, I., Salakhutdinov, R., 2014. Dropout: a simple way to prevent neural networks from overfitting. The journal of machine learning research 15, 1929–1958.
- Tölle, M., Laves, M.H., Schlaefer, A., 2021. A Mean-Field Variational Inference Approach to Deep Image Prior for Inverse Problems in Medical Imaging. Medical Imaging with Deep Learning , 698–713URL: https://openreview.net/forum?id=DvV%5C_b1KLb4.
- Vaswani, A., Shazeer, N., Parmar, N., Uszkoreit, J., Jones, L., Gomez, A.N., Kaiser, L., Polosukhin, I., 2017. Attention is all you need. arXiv preprint arXiv:1706.03762.
- Vercauteren, T., Pennec, X., Perchant, A., Ayache, N., 2009. Diffeomorphic demons: Efficient non-parametric image registration. NeuroImage 45, S61–S72.
- Viola, P., Wells III, W.M., 1997. Alignment by maximization of mutual information. International journal of computer vision 24, 137–154.
- Vishnevskiy, V., Gass, T., Szekely, G., Tanner, C., Goksel, O., 2016. Isotropic

- total variation regularization of displacements in parametric image registration. *IEEE transactions on medical imaging* 36, 385–395.
- de Vos, B.D., Berendsen, F.F., Viergever, M.A., Sokoooti, H., Staring, M., Işgum, I., 2019. A deep learning framework for unsupervised affine and deformable image registration. *Medical image analysis* 52, 128–143.
- de Vos, B.D., Berendsen, F.F., Viergever, M.A., Staring, M., Işgum, I., 2017. End-to-end unsupervised deformable image registration with a convolutional neural network, in: *Deep learning in medical image analysis and multimodal learning for clinical decision support*. Springer, pp. 204–212.
- Wang, D., Wu, Z., Yu, H., 2021a. Ted-net: Convolution-free t2t vision transformer-based encoder-decoder dilation network for low-dose ct denoising. *arXiv preprint arXiv:2106.04650*.
- Wang, W., Chen, C., Ding, M., Li, J., Yu, H., Zha, S., 2021b. Transbts: Multimodal brain tumor segmentation using transformer. *arXiv preprint arXiv:2103.04430*.
- Wang, W., Xie, E., Li, X., Fan, D.P., Song, K., Liang, D., Lu, T., Luo, P., Shao, L., 2021c. Pyramid vision transformer: A versatile backbone for dense prediction without convolutions. *arXiv preprint arXiv:2102.12122*.
- Wang, Z., Bovik, A.C., Sheikh, H.R., Simoncelli, E.P., 2004. Image quality assessment: from error visibility to structural similarity. *IEEE transactions on image processing* 13, 600–612.
- Wolberg, G., Zokai, S., 2000. Robust image registration using log-polar transform, in: *Proceedings 2000 International Conference on Image Processing (Cat. No. 00CH37101)*, IEEE, pp. 493–496.
- Xie, Y., Zhang, J., Shen, C., Xia, Y., 2021. Cotr: Efficiently bridging cnn and transformer for 3d medical image segmentation. *arXiv preprint arXiv:2103.03024*.
- Yang, X., Kwitt, R., Niethammer, M., 2016. Fast predictive image registration, in: *Deep Learning and Data Labeling for Medical Applications*. Springer, pp. 48–57.
- Yang, X., Kwitt, R., Styner, M., Niethammer, M., 2017a. Fast predictive multimodal image registration, in: *2017 IEEE 14th International Symposium on Biomedical Imaging (ISBI 2017)*, IEEE, pp. 858–862.
- Yang, X., Kwitt, R., Styner, M., Niethammer, M., 2017b. Quicksilver: Fast predictive image registration—a deep learning approach. *NeuroImage* 158, 378–396.
- Zhang, J., 2018. Inverse-consistent deep networks for unsupervised deformable image registration. *arXiv preprint arXiv:1809.03443*.
- Zhang, Y., Ma, J., Iyengar, P., Zhong, Y., Wang, J., 2017. A new ct reconstruction technique using adaptive deformation recovery and intensity correction (adric). *Medical physics* 44, 2223–2241.
- Zhang, Z., Yu, L., Liang, X., Zhao, W., Xing, L., 2021. Transct: Dual-path transformer for low dose computed tomography. *arXiv preprint arXiv:2103.00634*.
- Zhou, H.Y., Guo, J., Zhang, Y., Yu, L., Wang, L., Yu, Y., 2021. nnformer: Interleaved transformer for volumetric segmentation. [arXiv:2109.03201](https://arxiv.org/abs/2109.03201).
- Zhou, Z., Siddiquee, M.M.R., Tajbakhsh, N., Liang, J., 2019. Unet++: Redesigning skip connections to exploit multiscale features in image segmentation. *IEEE transactions on medical imaging* 39, 1856–1867.
- Zhu, B., Liu, J.Z., Cauley, S.F., Rosen, B.R., Rosen, M.S., 2018. Image reconstruction by domain-transform manifold learning. *Nature* 555, 487–492.